Chemical Society Reviews

TUTORIAL REVIEW

Chem. Soc. Rev., 2020, 49, 2869--2885 (DOI: 10.1039/c9cs00848a)

Synthesis, optoelectronic properties and applications of halide perovskites

Lata Chouhan,[1,†] *Sushant Ghimire,*[1,†] *Challapally Subrahmanyam,*[2] *Tsutomu Miyasaka,*[3,4] *Vasudevanpillai Biju*[1,*]

[1]Graduate School of Environmental Science and Research Institute for Electronic Science, Hokkaido University, Sapporo, Hokkaido 001-0020, Japan

[2]Deparment of Chemistry, Indian Institute of Technology Hyderabad, Kandi, Sangareddy, Telangana, India

[3]Faculty of Biomedical Engineering, Toin University of Yokohama, Yokohama, Japan

[4]Research Center for Advanced Science & Technology, the University of Tokyo, 4-6-1 Komaba, Meguro-ku, Tokyo 153-8904, Japan

[†]These authors equally contributed to this article.

**Address correspondence to: biju@es.hokudai.ac.jp*

TOC Graphic

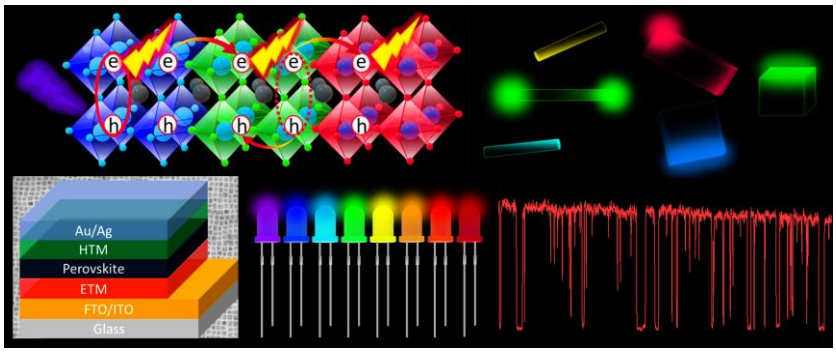

Abstract

Halide perovskites emerge into a class of most promising and cost-effective semiconductor materials for next generation photoluminescent, electroluminescent and photovoltaic devices. These perovskites own high optical absorption coefficient and narrow-band bright photoluminescence, which are in addition to halide-dependent tuneable bandgap, low exciton binding energy, and long-range carrier diffusion. These properties make perovskites superior

to classical semiconductors such as silicon. Most importantly, the simple synthesis of perovskites into high quality films, single crystals, nanocrystals and quantum dots attracts newcomers to develop novel perovskites with unique optoelectronic properties for optical and photovoltaic applications. Here, we comprehensively review recent advances in the synthesis and optoelectronic properties of films, microcrystals, nanocrystals and quantum dots of lead halide and lead-free halide perovskites. Followed by the classification of synthesis, we address the ensemble and single particle properties of perovskites from the viewpoints of the confinement and transport of charge carriers or excitons. Further, we correlate charge carrier properties of perovskite films, microcrystals, nanocrystals and quantum dots with the crystal structure and size, halide composition, temperature, and pressure. Finally, we illustrate the emerging applications of perovskites to solar cell, LED, and laser, and discuss the ongoing challenges in the field.

Key learning points

1) Synthesis of lead and lead-free halide perovskites: into films, microcrystals, nanocrystals, and quantum dots.
2) Halide-dependent tunable bandgap and luminescence properties.
3) Optoelectronic properties governed by excitons and charge carriers.
4) Photoluminescence blinking in films, microcrystals, nanoparticles and quantum dots.
5) Perovskites for high efficiency solar cells, bright LEDs and low threshold lasers.

1. Introduction

Since the discovery of the parental perovskite calcium titanate ($CaTiO_3$) by Gustav Rose in Ural Mountains, it took more than 150 years to optimize the properties of analogous halide perovskites and realize their practical applications. Halide perovskites become popular due to their cost-effective and simple synthesis, multicolor emission, high photoluminescence quantum yield (PLQY) and excellent excitonic and charge carrier properties. These properties attract perovskites to engineer devices such as LEDs,[1] lasers,[2] photodetectors,[3] and solar cells.[4] The general formula of halide perovskite is ABX_3 (Fig. 1a), where the A-site cation such as Cs^+, methylammonium ($CH_3NH_3^+$, MA) or formamidinium [$CH(NH)_2)_2^+$, FA] occupies the voids formed by the corner-sharing BX_6 octahedra. Isomorphs of halide perovskites are obtained by varying the A- or B-site cation (Pb^{2+}, Sn^{2+}, Ge^{2+}, Bi^{3+}, In^{3+} or Sb^{3+}) as well as halide ion ($X=Cl^-$, Br^-, I^-). Also, perovskites with mixed A-site and or B-site cations, such as

$MAFAPbX_3$, $KCsMAFAPbX_3$, Cs_2AgBiX_6, $Cs_2AgInCl_6$, and $Cs_2AgInBiX_6$ have been developed.

While the chemical composition dictates the crystal structure and stability of perovskites, the most attractive properties of these materials are halide- and size-dependent bandgap tuning and carrier confinement. PL color of perovskites is tuned (Fig. 1b and c) in the visible to near-infrared (NIR) region, which is through the preparation of mixed halide perovskites from mixed halide precursors or post-synthesis halide exchange reactions.[5,6] In general, chloride perovskites show violet to blue emission, which is green for bromide and deep-red to NIR for iodide samples. PL color can be tuned between the violet and green by increasing the composition of bromide in pure chloride perovskite or chloride in pure bromide perovskite. Similarly, PL color can be tuned between the green and NIR by mixing bromide and iodide ions. This halide-dependent tuning of emission color or bandgap originates from the modification of band-edge states formed by the hybridized *s* and *p* orbitals of halide and B-site cation. As the bandgap decreases from chloride to bromide and from bromide to iodide, the effective mass of exciton decreases. Thus, the exciton binding energy decreases from chloride to iodide, which modifies the excitonic and charge carrier lifetimes in perovskites. Other factors affecting the exciton binding energy are A-site cation and the size. Images of perovskites with different morphology, size, and chemical composition are shown in Fig. 1d-g.

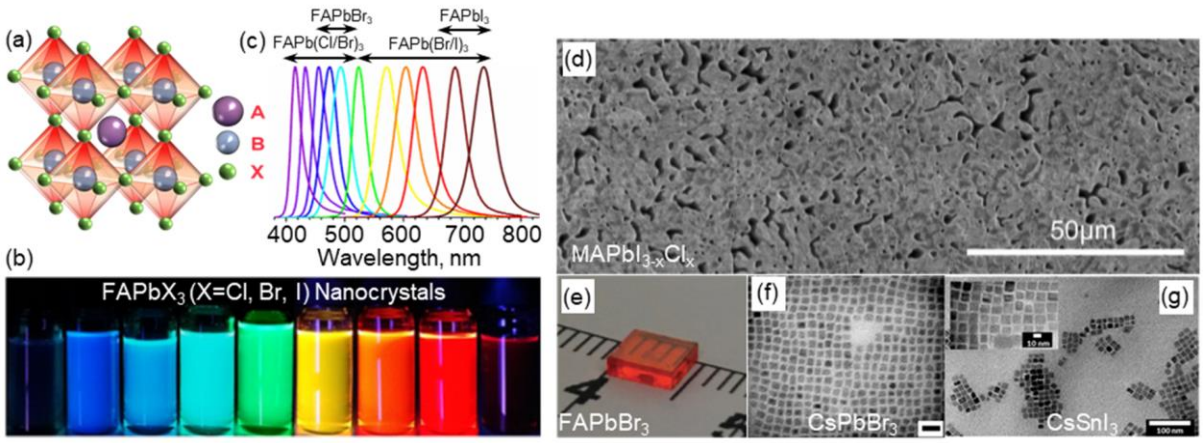

Fig. 1 Morphology and PL properties of halide perovskites. (a) The general structure of ABX_3 perovskite. (b) PL images and (c) PL spectra of colloidal solutions of $FAPbX_3$ perovskite nanocrystals. (d) A SEM image of a $MAPbI_{3-x}Cl_x$ perovskite film. (e) A photograph of a $FAPbBr_3$ single crystal. (f, g) TEM images of (f) $CsPbBr_3$ and (g) $CsSnI_3$ nanocrystals. Reproduced with permission from (b and c) ref. 6 (copyright 2017, American Chemical Society), (d) ref. 5 (copyright 2013, American Association for the Advancement of Science), (e) ref. 7 (copyright 2015, The Royal Society of Chemistry), (f) ref. 8 (copyright 2019, American Chemical Society), and (g) ref. 9 (copyright 2016, American Chemical Society).

In this review, we introduce newcomers to the synthesis, structure, and optical properties of perovskites with different size, structure, and composition. Further, we correlate the bandgap, and excitonic and charge carrier properties of these materials with perovskite solar cell, LED and laser.

2. Synthesis

The factors to be considered during the synthesis of halide perovskites are the size, structure, stability, anticipated optical and charge carrier properties, potential device applications, and toxicity. The stability of ABX_3 perovskite structure is determined by the Goldschmidt tolerance factor:

$$t = \frac{r_a + r_x}{\sqrt{2}\,(r_b + r_x)} \quad (1)$$

and the octahedral factor $\mu = r_b/r_x$, where r_a, r_b and r_x respectively are the radii of A-site cation, B-site cation and halide ion.[10] For the stable perovskite structure, the tolerance factor should be in between 0.81 and 1.00, and the octahedral factor should be in between 0.44 and 0.9, which are determined by the sizes of cation and anion. Based on the above stability factors, MA-, FA-, and Cs-based halide perovskites are the most stable structures synthesized in laboratories. While lead perovskites show excellent optical and electronic properties, the environmental cost of it, particularly toxicity to aquatic and terrestrial life, attracted researchers to replace lead by other metal ions such as Sn^{2+}, Ge^{2+}, Cu^{+}, Ag^{+}, Bi^{3+}, Sb^{3+}, or In^{3+}. Among these ions, Sn^{2+} renders perovskites with properties like Pb^{2+}. However, Sn^{2+} gets oxidized into Sn^{4+} and as the result, the geometry of the perovskite distorts and the optical and electronic properties change. Thus, perovskites based on other B-site cations such as Sb^{3+} are prepared and studied.[11] These cations form $A_3B_2X_9$ configuration due to the distortion of BX_6 network caused by their small size. Yet another type of lead-free halide perovskite is $A_2B^{'}B^{''}X_6$ double perovskites.[12] To fulfil the valency, double perovskites require trivalent and monovalent cations chosen from among Cu^{+}, Ag^{+}, Bi^{3+}, Sb^{3+} and In^{3+}. While A- and B-site cations play significant roles on the stability of perovskites, optical and charge carrier properties are controlled by halide ions and the size. Fig. 2 summarizes the methods for the synthesis of halide perovskites into thin films, microcrystals, nanocrystals and quantum dots (QDs) with different A- and B-site cations and halide ions.

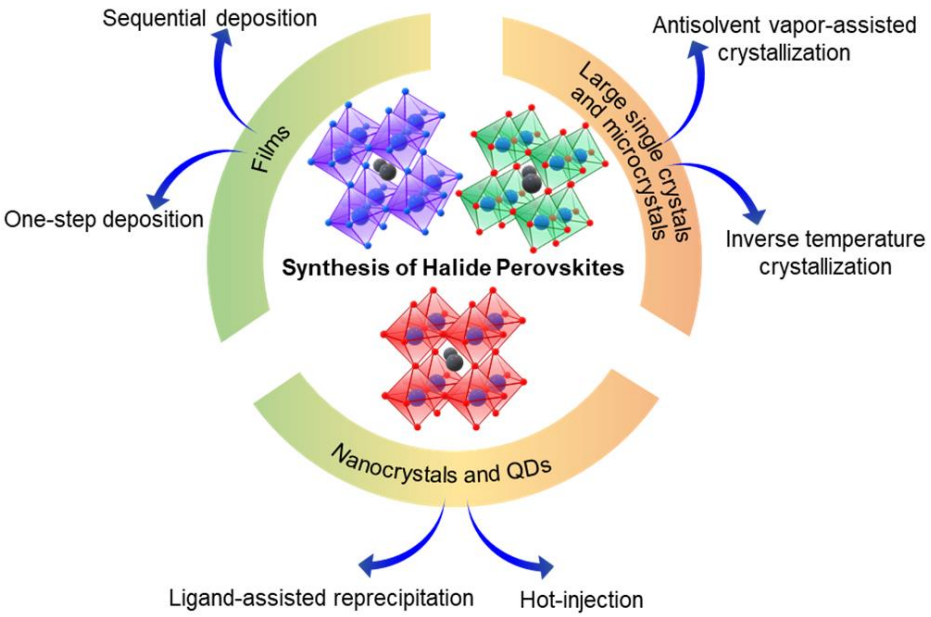

Fig. 2 Preparation of perovskite thin films, microcrystals, nanocrystals and QDs.

2.1. Films

High quality perovskite films are light absorbing layers in perovskite solar cells (PSCs). Such films are fabricated in single[4,13-15] step or two steps[16] from the solution of their precursor salts (MAX, FAX or CsX and PbX_2) dissolved in solvents such as dimethyl formamide (DMF), dimethyl sulfoxide (DMSO) or γ-butyrolactone (GBL). These solvents enable slow crystal nucleation and growth of perovskites, which is owing to the low vapor pressures and high boiling temperatures. For instance, a $MAPbX_3$ perovskite film is prepared by simply depositing a precursor solution of MAX and PbX_2 in DMF or GBL on a substrate (Fig. 3a). Antisolvent-assisted deposition, vacuum- and gas-pumping, and hot-casting are other methods for the preparation of uniform perovskite layers in PSCs. Spiccia and co-workers[15] used antisolvent-induced fast crystallization of $MAPbI_3$ to form a micro-crystalline film free from grain-boundaries. Here, a precursor solution of $MAPbI_3$ in DMF is spin-coated on TiO_2, which is followed by exposing the film to the antisolvent dichlorobenzene. Similarly, polycrystalline thin films of $MASnX_3$ perovskites are prepared by spin-coating of stoichiometric amounts of MAI and SnI_2 dissolved in degassed DMF on TiO_2 or Al_2O_3.[13]

In two-step or sequential deposition of perovskite layers (Fig. 3a), heterogenous reaction takes place between the solutions of PbX_2 and the organic or inorganic halide salt. For example, a film of mesoporous TiO_2 is deposited on the compact thin layer of TiO_2, which is followed by the spin-coating of PbI_2 dissolved in DMF. After the drying of the PbI_2 solution, MAI is spin-coated and annealed at 100 °C for 20 s to provide a thin film of $MAPbI_3$ cuboids.[16]

Compositional engineering of perovskite crystals using mixed cations and halide ions in one-step coating provides uniform pinhole-free perovskite films of high efficiency PSCs. Uniform perovskite layers are prepared by spray-coating, soft-cover deposition, brush painting, screen-printing, inkjet printing, blade-coating, or slot-die coating.[17] Among these methods, blade-coating is widely used in the fabrication of TiO_2 mesoporous thin film in dye-sensitized and QD-sensitized solar cells and it gains popularity in the deposition of large area perovskite PSCs. In this method, a perovskite precursor solution is swiped on a pre-heated substrate and kept for solvent evaporation. However, the preparation of uniform films over a large coverage area are often challenged by uneven edges of the blade. The speed of blade swiping is another important factor to be considered in the preparation of uniform films, as the speed directs the fluid dynamics and the rate of solvent evaporation. Typical example of blade-coating is the preparation of a $MAPbI_3$ perovskite film on a layer of poly(bis(4-phenyl) (2,4,6-trimethylphenyl)amine) (PTAA).[18] First, PTAA is blade-coated on an indium tin oxide (ITO)/glass substrate, which is followed by annealing this layer and blade-coating (50 mms^{-1}) of a $MAPbI_3$ perovskite solution supplemented with the surfactant l-α -phosphatidylcholine. The use of perovskite films in solar cells is reviewed in section 6.1.

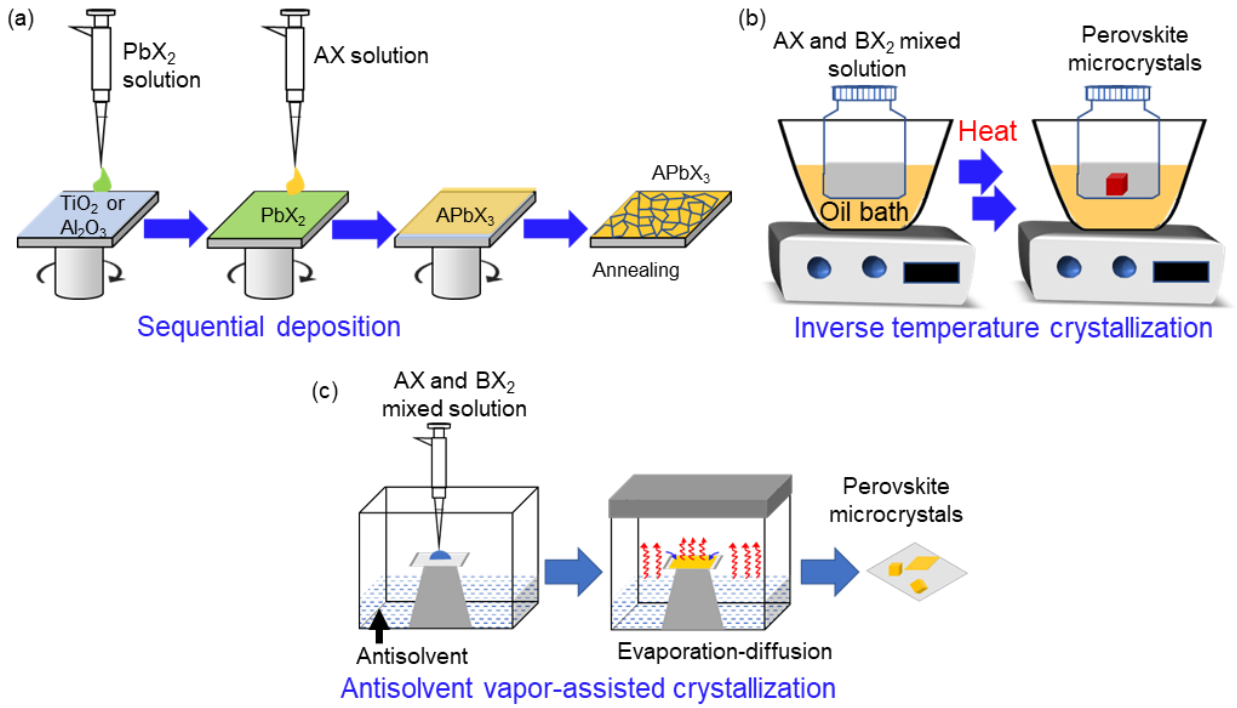

Fig. 3 General methods for the synthesis of (a) films and (b,c) crystals of perovskites. (a) Sequential deposition of precursor solution. (b) inverse temperature crystallization, and (c) antisolvent vapor-assisted crystallization.

2.2. Large Single Crystals and Microcrystals

Various processes in the synthesis of single crystals of halide perovskites include inverse temperature crystallization (ITC, Fig. 3b), antisolvent vapor-assisted crystallization (AVC, Fig. 3c), and vapour phase melt approach. In ITC, the retrograde solubility of halide perovskites helps in the synthesis of millimetre size crystals. For example, single crystals of $FAPbI_3$ are prepared by controlling the temperature of its precursor (PbI_2 and FAI) solution in GBL, which is in the range of 80 to 120 ℃. Similarly, large single crystals of $FAPbBr_3$ can be grown by increasing the temperature of a precursor solution composed of $PbBr_2$ and FABr in a mixture (1:1 v/v) of DMF and GBL.[7] Here, GBL helps in the crystal growth by lowering the solubility of precursors. Common antisolvents used in the preparation of perovskite microcrystals are chlorobenzene, ethyl acetate and dichloromethane. $MAPbX_3$ microcrystals are prepared by the slow diffusion of dichloromethane into a precursor solution containing stoichiometric amounts of MAX and PbX_2 in DMF.[19] In vapor-phase melt approach, powders of CsX and PbX_2 are kept inside a quartz tube in a furnace where the temperature is slowly raised to 600 ℃ and kept at the this temperature for 15 min to grow the crystals.[20] Recently, lead-free double perovskite crystals are prepared by different methods such as hydrothermal crystallization and precipitation. For example, polycrystalline Cs_2AgBiX_6 double perovskites are prepared by the addition of AgX and BiX_3 into a solution of HX and H_3PO_2 at 120 ℃.[12]

2.3. Nanocrystals and Quantum Dots

The growth of perovskite crystals can be confined to the nanometer scale by surface capping using long-chain organic ligands which are aliphatic carboxylic acids and amines. Perovskite nanoparticles (or nanocrystals) are routinely prepared by the hot injection or ligand-assisted reprecipitation (LARP) method shown in Fig. 4. The size and morphology of nanocrystals, such as nanocube, nanowires, nanoplateles and QDs, is determined by the chain length of the ligands and the reaction temperature. In typical synthesis of $CsPbBr_3$ perovskite nanocrystal by the hot-injection method, caesium acetate and oleic acid are dissolved in hexadecene at 120 ℃, and in parallel, a mixture of $PbBr_2$ and capping ligands such as oleic acid and hexadecyl amine are dissolved in hexadecene at 120 ℃. Then, the hot solution of caesium acetate is injected into the $PbBr_2$ solution at 170 ℃. Immediately after the injection, the reaction solution is cooled in an ice bath, and nanocrystals are collected by centrifugation.[8] Similarly, $FAPbBr_3$ nanocrystals are synthesized at 130 ℃ by injecting a solution of octadecylammonium bromide in toluene to a solution of lead acetate, formamidinium acetate and oleic acid in octadecene. The reaction is quenched after 10 s, and $FAPbBr_3$ nanocrystals are collected by purification of the reaction

mixture using toluene and acetonitrile.[21] LARP method is convenient for the preparation of perovskite nanocrystals at room temperature. $MAPbBr_3$ nanocrystals are prepared by the dropwise addition of a solution of MABr and $PbBr_2$ in DMF into a mixture of octylamine and oleic acid dissolved in toluene and under vigorous stirring.[22]

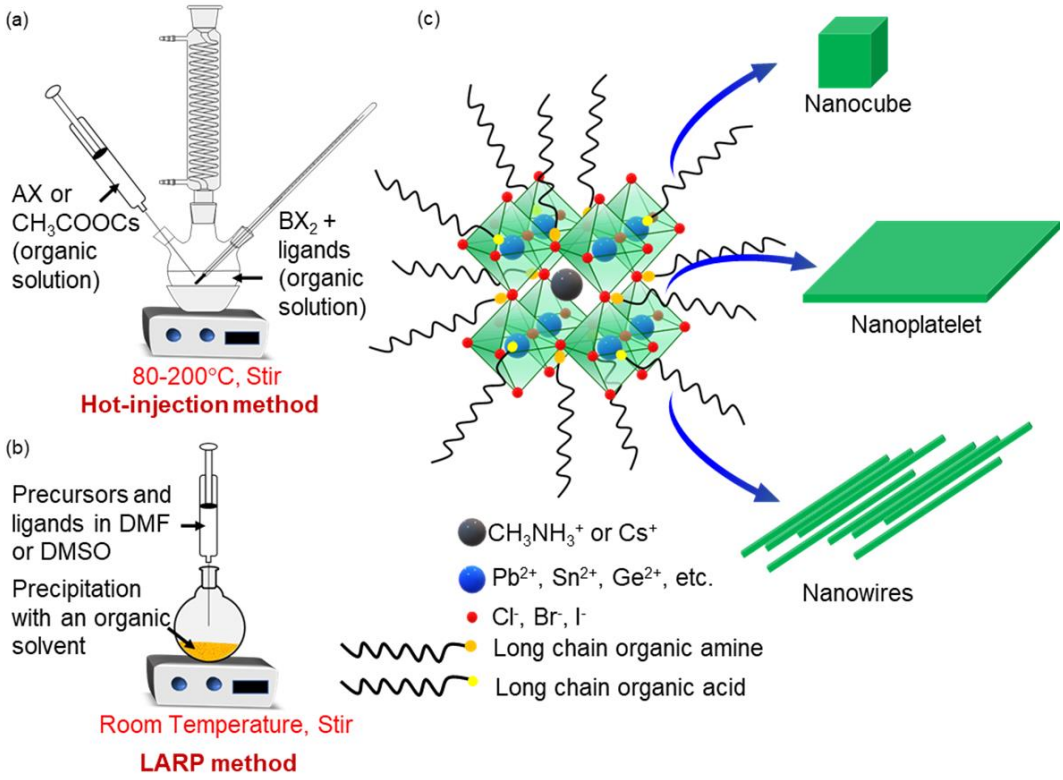

Fig. 4 (a,b) Synthesis of perovskite nanocrystals by (a) hot-injection method and (b) LARP method. (c) Ligand-capped nanocrystals of perovskites with different morphologies.

Nanocrystals of lead-free perovskite are synthesized by the hot injection or LARP method like their lead-based counterparts. For example, $CsSnX_3$ nanocrystals are prepared by suspending Cs_2CO_3 in a mixture of oleic acid and oleylamine in octadecene, which is followed by injecting SnX_2 dissolved in tri-*n*-octylphosphine and increasing the temperature of the solution to 100~170 °C.[9] Here, $CsSnX_3$ nanocrystals precipitate out upon cooling of the reaction mixture in an ice-bath. LARP method is useful for the synthesis of lead-free $A_3M_2X_9$ perovskite nanocrystals at room temperature. For example, $Cs_3Sb_2Br_9$ QDs are prepared by mixing CsBr and $SbBr_3$ together in DMF (or DMSO) supplemented with octadecyl amine or *n*-octylamine, and quickly adding a mixture of octane and oleic acid. $Cs_3Sb_2Br_9$ QDs are collected from the reaction solution by the addition of acetone or octane and centrifugation. $Cs_3Sb_2Cl_9$ and $Cs_3Sb_2I_9$ QDs are prepared by halide exchange in $Cs_3Sb_2Br_9$ using CsX (X= Cl, I) dissolved in DMSO.[11] More recently, 2-6 nm size $Cs_2AgIn_xBi_{1-x}Cl_6$ double perovskites are

synthesized by antisolvent-assisted recrystallization in a mixture of oleic acid and isopropanol.[23] Here, precursor solutions of cations are prepared by dissolving CsCl, AgCl, $BiCl_3$ and $InCl_3$ in DMSO, and the composition of B-site cations is varied by using different molar ratios of $BiCl_3$ and $InCl_3$.

3. Crystal Structure

The composition, crystal phase and unit cell parameters of perovskites are characterized by single crystal and powder X-ray diffraction (XRD) analysis. Halide perovskites show different crystal structures and phases such as cubic, orthorhombic, trigonal, monoclinic, pseudocubic, hexagonal and tetragonal (Table 1). XRD patterns of $MAPbBr_3$, $CsPbX_3$ and Sn-based

Table 1: Phases and groups of halide perovskites (RT: room temperature).[6,9,11,12,19,23-26]

Perovskite	Halide	Phase	Group	Temperature	Reference
$MAPbX_3$	Br, I	Cubic	*Pm3m*	RT 80°C for Br	*19* *25* *26*
		Tetragonal	*I4/mcm or I4/m*	110°C for I	*19* *25*
	I	Pseudocubic	*P4mm*	RT	*25*
$FAPbX_3$	Cl, Br, I	Cubic	-	RT	*6*
$CsPbX_3$	Cl, Br, I	Cubic	*Pm3m*	120-200°C	*24*
	I	Orthorhombic	*Pnma*	315°C	*24*
$CsSnX_3$	Br, I	Orthorhombic	*Pnam*	170°C	*9*
	Cl	Cubic	*Pm3m*	170°C	*9*
$Cs_3Sb_2X_9$	Br	Trigonal	$P\bar{3}m1$	90°C	*11*
Cs_2AgBiX_6	Cl, Br	Cubic	$Fm\bar{3}m$	150-210°C	*12*
$Cs_2AgIn_xBi_{1-x}X_6$	Cl	Cubic	$Fm\bar{3}m$	RT	*23*

perovskites are shown in Fig. 5. Different crystal phases are assigned according to the Miller indices. The prominent Miller indices of cubic phase are (001), (011), (002) and (021) which are seen at 2θ ca 15°, 22°, 30° and 34°, respectively. The difference between cubic and orthorhombic phases is assigned based on two additional peaks ca 30°. Organic-inorganic hybrid perovskites form stable cubic phase at high temperatures, which is due to the reduced degree of rotational movement of A-site organic cation. When the temperature is decreased, the phase transforms into tetragonal and orthorhombic phases. The Miller indices can be calculated from Bragg's law, $n\lambda = 2d_{hkl}sin\theta$, where d_{hkl} is the interplanar spacing and λ is the

XRD wavelength. The interplanar spacing depends on the lattice constants which are different for different unit cells. Different structural forms of perovskites, such as large single crystals, thin films, nanocrystals, nanocubes, nanoplatelets, nanowires, QDs, quantum cubes, and nanosheets can be characterized using XRD.

XRD data help one to analyse the crystal phase and chemical composition of perovskites. When compared with single crystal (Fig. 5a), the diffraction peaks of nanocrystals are slightly shifted to the small 2θ angle (Fig. 5b). Further, in single and mixed halide compositions, the diffraction peak shifts from the large to small 2θ angle while going from chloride to bromide and bromide to iodide.[24] The lattice contraction becomes larger down the halide group, and the corresponding changes can be assigned to the shifting, appearance (ca 35°, 27°, and 48°) and disappearance (ca 52°) of some of the diffraction peaks (Fig. 5b and c).[9,24] Mixed halide perovskites show slight shift in the diffraction peaks, when compared to single halide perovskites. For example, the diffraction angle increases while increasing the ratio of chloride in a chloride-bromide mixed perovskite.

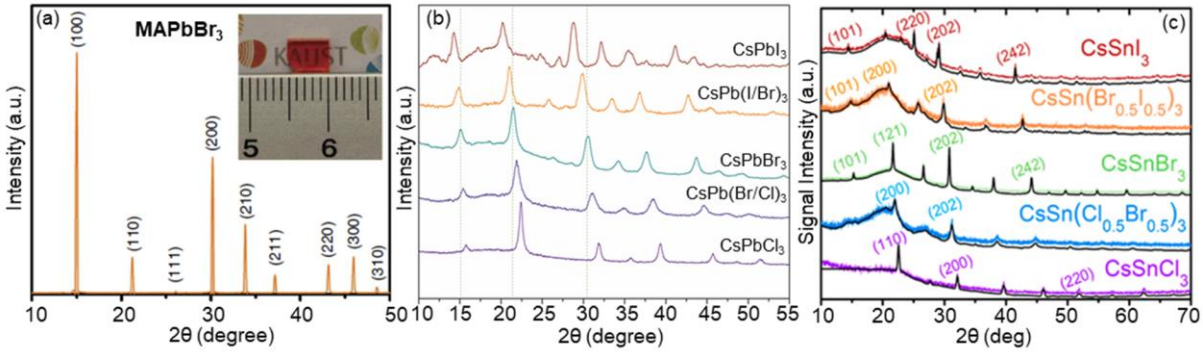

Fig. 5 XRD of (a) $MAPbBr_3$ single crystal, and (b) $CsPbX_3$ and (c) $CsSnX_3$ nanoparticles. Reproduced with permission from (a) ref. 26 (copyright 2015, Nature Publishing Group), (b) ref. 24 (copyright 2015, American Chemical Society), and (c) ref. 9 (copyright 2016, American Chemical Society).

4. Energy States

The appealing optical and charge carrier properties of perovskites emerge from the unique distribution of energy states at the band-edge. Being direct bandgap semiconductors, with the exception of noncentrosymmetric distribution of conduction band minimum (CBM) and valence band maximum (VBM) induced by Rashba effect and Dresselhaus splitting, the band-edge of halide perovskites is composed by antibonding atomic orbitals of $[BX_6]^{4-}$ octahedra.[10,27] Here, CBM is constituted by the sigma (σ^*) and pie (π^*) antibonding orbital, which are formed by the hybridization of 6*p*-orbitals of lead and *s*- and *p*-orbitals of halides, respectively (Fig.

6a). On the other hand, *6s*- and *6p*-orbitals of lead and *s*- and *p*-orbitals of halide contribute to VBM.

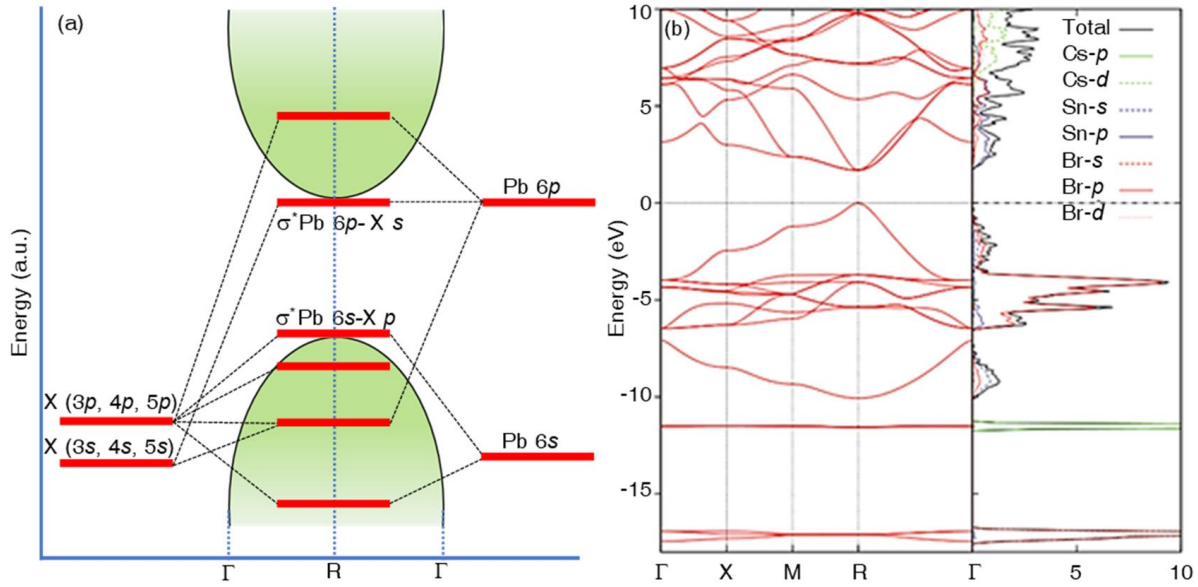

Fig. 6 (a) Band-edge states of halide perovskites without considering spin-orbit coupling (SOC). (b) Band structure and partial density of states of $CsSnBr_3$ perovskite. Fig. b is reproduced with permission from ref. 27 (copyright 2013, American Physical Society).

Lead-free perovskites show similar band-edge structure like lead perovskites (Fig. 6b). For instance, in cubic $CsSnBr_3$ perovskite, VBM antibonding state is a mixture of *4p*-orbitals of Br and *5s*-orbital of Sn, whereas CBM is mainly constituted by 5*p*-orbitals of Sn.[27] Here, VBM is nondegenerate while CBM is three-fold degenerate without any contribution from SOC. When SOC becomes significant, the degeneracy of CBM is broken, and it splits into spin–orbit split-off doublet states and quadruplet states. Optically allowed transitions from the VBM to the spin–orbit split-off states and quadruplet states render fine optical absorption features to halide perovskites. Also, an increase in the dispersion of conduction band through SOC-assisted splitting lowers the optical bandgap and affects charge carrier and PL properties. In fact, SOC which tunes the optical properties of perovskites is associated with other factors such as the composition, octahedral tilt, and temperature.

4. Optoelectronic Properties

4.1. Charge Carrier Dynamics

The generation, dynamics and recombination of charge carriers and excitons in perovskites largely depend on the composition, crystal structure, and size. Photogenerated charge carriers in perovskites are either freely diffusing or excitonically bound, depending on the exciton

binding energy. The dynamics of free carriers is characterized by the diffusion coefficient ($D_{n,p}$) and carrier mobility ($\mu_{n,p}$), which are related through the Einstein equation,

$$\mu_{n,p} = eD_{n,p}/k_BT \quad (2)$$

where e is electronic charge, k_B is Boltzmann constant and T is temperature. These parameters are related to the electronic structure through the effective mass (m^{eff}) of carriers. The comparable m^{eff} of electron and hole in halide perovskites provides this class of materials with balanced electron and hole diffusion lengths. Although different theoretical and experimental methods provide slightly different m^{eff} values to electrons and holes, the main factors that affect the masses are SOC, chemical composition, and the size. The diffusion length (L_D) of charge carriers is related to their mobility or diffusion coefficient by the equation,[29]

$$L_D=(k_BT\mu_{n,p}\,\tau/e)^{1/2}= (D_{n,p}\,\tau)^{1/2} \quad (3)$$

where, τ is PL lifetime. High mobility and long lifetime of charge carriers result in long L_D, which is an important requirement for perovskites to be an efficient charge transport layer in photovoltaics. The long PL lifetimes of single crystal and thin film perovskites show the presence of free carriers formed by the dissociation of photogenerated excitons, when the thermal energy (k_BT) overcomes the exciton binding energy.

Charge carrier recombination dynamics in perovskites is explained using the following rate equation

$$-\frac{dn}{dt} = k_1n + k_2n^2 + k_3n^3 \quad (4)$$

where, k_1, k_2, and k_3 are the rate constants of monomolecular, bimolecular and Auger recombinations, and n is the total carrier concentration. The monomolecular recombination is a geminate type excitonic recombination or a trap-assisted recombination. On the other hand, bimolecular recombination is non-geminate recombination of free charge carriers. In Auger recombination, the charge carriers transfer the energy or momentum to a third charge carrier. These recombination mechanisms in perovskites contribute to the total recombination rate and influence the carrier lifetime and diffusion length. The monomolecular recombination in perovskite is mainly governed by the trap-assisted processes, and it depends on the energy, density, and distribution of trap states. Furthermore, the monomolecular recombination rate is influenced by material purity and crystallinity. The trap-assisted recombination rate is in the order of 10^6 s^{-1} for single and mixed halide lead perovskites.[30,31] On the other hand, for lead-free $MASnI_3$ perovskites, the monomolecular recombination rate (~10^9 s^{-1}) is three orders of magnitude greater than $MAPbI_3$, which is attributed to the self-doping by Sn^{+4} ions.[13] The activation energy and depth of traps depend on the crystalline phase of perovskites, and thus

affect the monomolecular recombination rate. For example, the trap-assisted recombination rate is higher in cubic and tetragonal phases than orthorhombic phase, which is due to the difference in activation energies of trap formation in these phases.[30]

Bimolecular recombination in perovskites depends on the composition of halide and metal ions. The ratio of bimolecular recombination rate constant to the charge carrier mobility is lower than predicted by the Langevin theory, according to which the bimolecular recombination occurs when electrons and holes move within their coulombically-bound radius. Hence, the deviation from Langevin theory in perovskites refers to a low bimolecular recombination rate with high carrier mobility. The non-Langevin bimolecular recombination behaviour in perovskite is attributed to the occupation of different molecular orbitals in perovskite unit cell by an electron and a hole, which are formed by the overlapping of energetically different *s*- and *p*-orbitals of halide and metal ions (Pb, Sn). The bimolecular recombination rate largely varies in perovskite single crystals and films. For example, perovskites composed of lighter halides (Br instead of I) and metals (Sn instead of Pb) show larger bimolecular recombination rates. Such variations of rate with chemical composition are associated with the modification of band structure and exciton binding energy.

While trap-assisted and bimolecular recombination in perovskites are important phenomena under intermediate charge carrier density and one sun illumination, Auger-assisted nonradiated recombination processes become important under high carrier concentrations. The rate of Auger-assisted recombination is high in orthorhombic phase at low temperature, whereas it remains low in high temperature tetragonal and cubic phases.[30] This phase-specific variation of the rate is due to varying degrees of SOC and hydrogen bonding. Auger recombination rate is also influenced by the presence of impurities and phonons. The above carrier recombination dynamics affect the PL lifetime of perovskites. PL lifetime of nanocrystals varies from sub-nanosecond to several ten nanoseconds, which largely depends on quantum confinement, whereas it scales up from sub-microsecond to sub-millisecond in bulk single crystals. For example, $MAPbI_3$ single crystals show carrier lifetime as long as 234 μs (Fig. 7a).[29] Perovskite thin films also show long carrier lifetimes and diffusion lengths (Fig. 7b and c).[5,8,31]

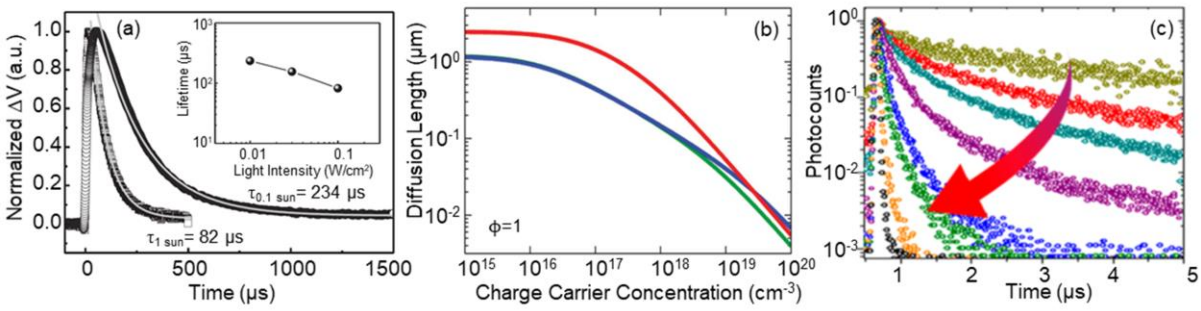

Fig. 7 Charge carrier properties of perovskites. (a) Transient photovoltaic data of $MAPbI_3$ perovskite showing long carrier lifetimes. (b) Diffusion length with respect to charge carrier density. (c) PL decay profiles of $MAPbBr_3$ perovskite with increasing intensity of excitation light. Reproduced with permission from (a) ref. 29 (copyright 2015, American Association for the Advancement of Science), (b) ref. 31 (copyright 2014, Wiley-VCH Verlag GmbH & Co. KGaA, Weinheim), and (c) ref. 8 (copyright 2019, American Chemical Society).

4.2. Absorption and Photoluminescence

Absorption and photoluminescence of perovskites are tuned in the UV, visible and NIR regions by varying the composition of halides from Cl to I. Since VBM of perovskites is formed by the mixing of halide *p*-orbitals and metal *s*- orbital, the halogen *p*-character in VBM can be increased by changing halide ion from Cl^- to Br^- and from Br^- to I^-, and as a result SOC increases.[10,27] Therefore, by changing halide ion from Cl^- to I^-, the bandgap decreases and PL spectrum shifts to the red as shown in Fig. 8a.[24] The octahedral tilt[32] is another factor that modifies the PL properties of perovskites, which occurs due to decrease of Pb-X-Pb dihedral angle upon replacement of a large A-site cation (FA^+) with a smaller one (Cs^+). Bandgap variation with octahedral tilt is shown in Fig. 8b.[32] Similarly, the change of crystal structure from cubic to tetragonal or other phases causes an octahedral tilt. Such a tilt in PbX_6 octahedra weakens SOC by lowering orbital overlap between Pb and X, which in turn increases the bandgap and shifts the PL band to the blue. Also, the cation size and hydrogen bonding of MA^+ or FA^+ ion with $[PbX_6]^{4-}$ octahedra influence the electronic and optical properties of perovskites by altering the covalent or ionic character of Pb-X bond.[32] Tetragonal-to-pseudocubic structural change, which is by changing A-site cation from MA^+ to FA^+, increases the hydrogen bond between FA^+ and $[PbX_6]^{4-}$. This in turn increases the ionic character of Pb−X bond and the contribution of Pb character to CBM. SOC becomes stronger in stable pseudocubic structure than octahedrally tilted tetragonal structure, resulting in a decrease of bandgap. The bandgap energies of different crystalline phases of Cs, MA and FA perovskites are given in Fig. 8c.[32]

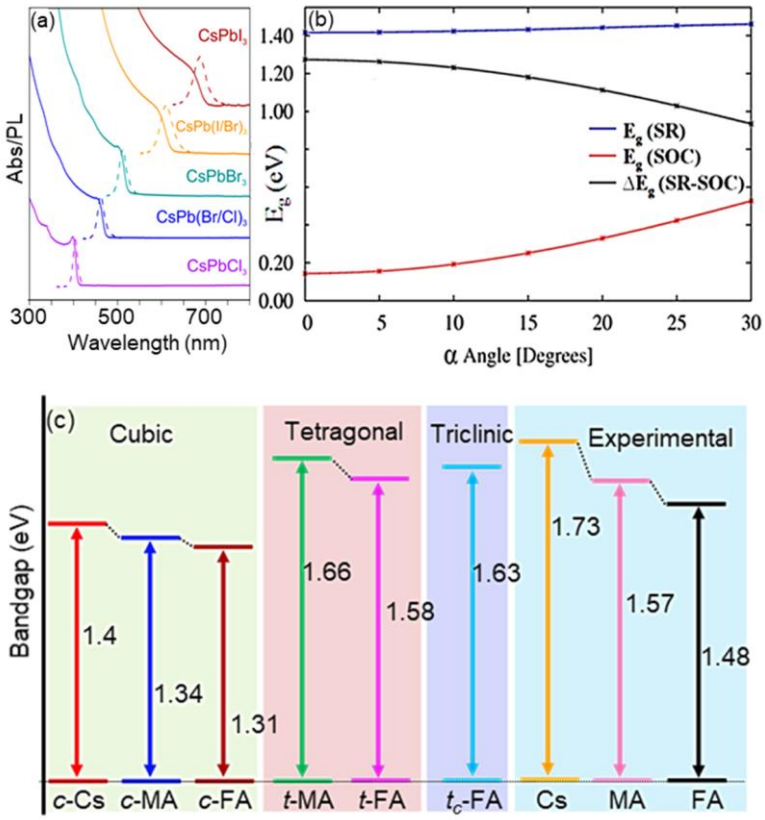

Fig. 8 The effect of anion and cation on optical properties of perovskites. (a) Absorption and PL spectra of $CsPbX_3$ nanoparticles with different halide compositions. (b) Calculated variations of bandgap in $CsPbI_3$ through octahedral tilt. (c) Calculated bandgap energies of cubic (*c*), tetragonal (*t*) and triclinic (t_c) phases of $APbI_3$ (A=Cs/MA/FA) perovskites. Reproduced with permission from (a) ref. 24 (copyright 2015, American Chemical Society), and (b) ref. 32 (copyright 2014, American Chemical Society).

The size is another factor that controls optoelectronic properties of perovskites. Decrease in size below the exciton Bohr radius renders quantum confinement effect to perovskites, evidenced by the appearance of sharp excitonic peaks, narrow PL bands, and blue-shifted absorption and PL spectra.[6,28,33-35] As shown in Fig. 9a, the gradual blue-shift of the absorption onset with decrease in crystal size (from 6.2 to 3.7 nm), which is correlated with the blue-shift of emission peaks, are characteristics of quantum confinement effect in $CsPbBr_3$ perovskites.[33] The size and bandgap of $MAPbX_3$ are correlated in Fig. 9b.[34] Similarly, as shown in Fig. 9c and d, quantum confinement effect is observed in perovskite nanoplatelets and nanowires. Apart from the size, the composition of halogen plays important roles on quantum confinement. For example, exciton Bohr radius of $CsPbX_3$ perovskites varies as 2.5 nm for $CsPbCl_3$, 3.5 nm for $CsPbBr_3$ and 6 nm for $CsPbI_3$.[24]

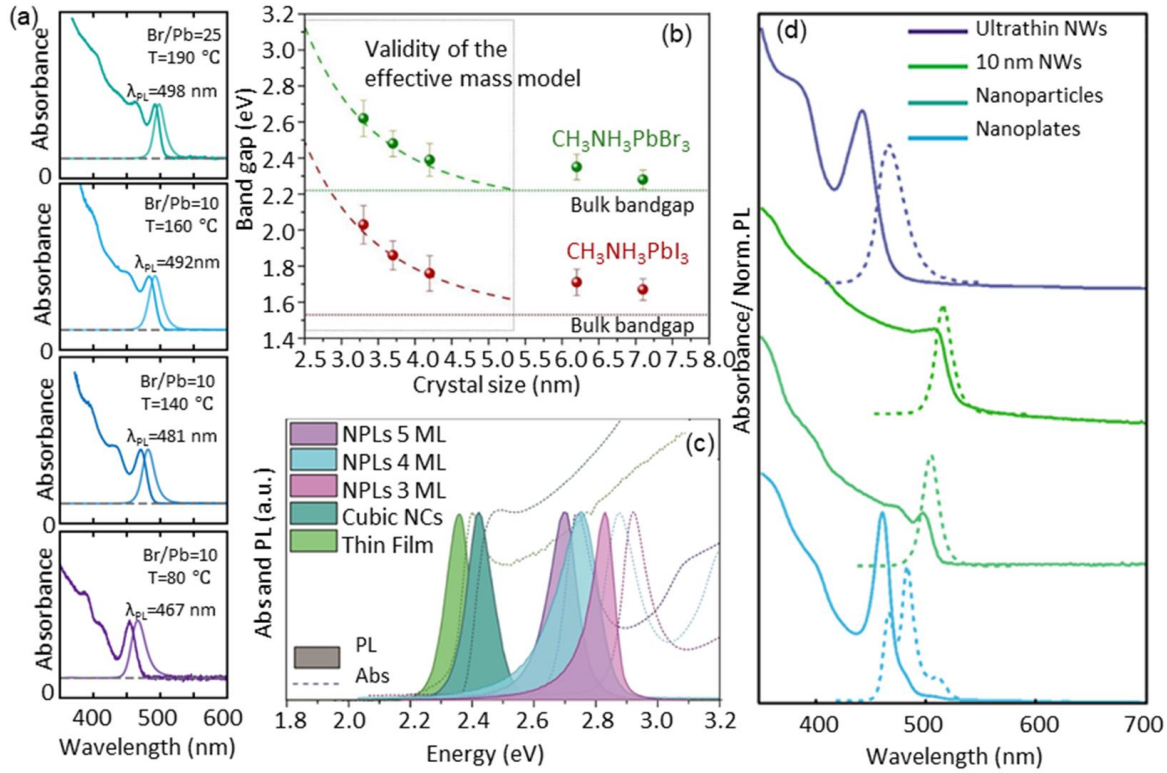

Fig. 9. The effect of size and shape on optical properties of perovskites. (a) Size-dependent absorption and PL spectra of $CsPbBr_3$ perovskites. (b) Experimental and theoretical bandgap values as a function of nanocrystal size. (c,d) Absorption and PL spectra of $CsPbBr_3$ perovskite nanocrystals with different shapes. Reproduced with permission from (a) ref. 33 (copyright 2018, American Chemical Society), (b) ref. 34, (copyright 2016, American Chemical Society), (c) ref. 28 (copyright 2016, American Chemical Society), and (d) ref. 35 (copyright 2016, American Chemical Society).

Temperature and pressure also affect the absorption and PL properties of perovskites. The role of temperature is to induce phase transition and vary exciton-phonon interactions by thermal expansion.[30] As the temperature of a perovskite crystal is increased, a series of structural changes or phase transitions occur. In lead iodide perovskites (Fig. 10a), variation of PL properties occurs in three distinct regimes, orthorhombic (low temperature), tetragonal (room temperature), and cubic (high temperature) phases.[30] Such a phase transformation affects the PL properties by altering the SOC through octahedral tilt. With increase in temperature, a perovskite crystal tends to stabilize in the cubic phase which renders minimal octahedral tilt and strong SOC. Consequently, the bandgap decreases and the absorption and PL spectra red-shift. Further, the broadening of absorption and PL spectra observed at higher temperatures is attributed to enhanced exciton-phonon interactions. Like temperature, pressure modifies the structure as well as electronic and optical properties of perovskites.[36] Here, the role of pressure is to alter the SOC through pressure-induced compression of Pb-X bond, shrinkage of Pb-X-

Pb angle or increase in octahedral tilt, and amorphization of crystal lattice. As shown in Fig. 10b, pressure-induced changes in optical properties of $FAPbBr_3$ perovskites are associated with structural changes [cubic ($Pm\bar{3}m$) → cubic ($Im\bar{3}$) → orthorhombic ($Pnma$)].[36]

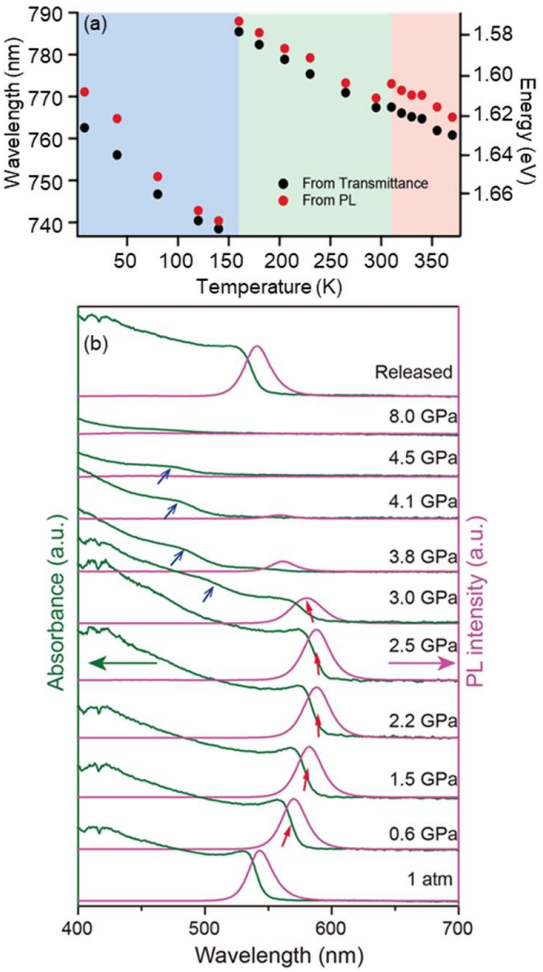

Fig. 10 The effect of temperature and pressure on optical properties of halide perovskites. (a) Temperature-dependent PL of different phases of $MAPbI_3$ perovskites. (b) Pressure-dependent PL of $FAPbBr_3$ perovskites. Reproduced with permission from (a) ref. 30 (copyright 2015, Wiley-VCH Verlag GmbH & Co. KGaA, Weinheim), and (b) ref. 36 (copyright 2016, American Chemical Society).

5. Photoluminescence Blinking

Single-molecule micro-spectroscopy, which is widely used in the field of cadmium and lead chalcogenide QDs is helpful for obtaining insight into the properties of perovskites at the single particle level. Single particle studies reveal PL characteristics of perovskites thin films,[37] microcrystals,[38] nanocrystals[38-40] and QDs.[41,42] Blinking is characterized by a sequence of stochastic bright (ON) and dark (OFF) events (Fig. 11),[38] which are due to the repeated radiative and nonradiative recombination of photogenerated excitons or charge carriers.

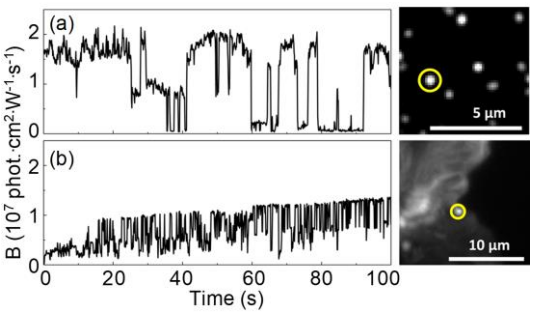

Fig. 11 PL blinking in halide perovskites. (left) PL intensity trajectories in the unit of brightness and (right) PL images of (a) a $MAPbI_3$ nanocrystal and (b) localized emitting site located on the top of a large $MAPbI_3$ crystal. Reproduced with permission from ref. 38 (copyright 2015, American Chemical Society).

Halide perovskites show different PL blinking behaviours (Figs. 11 and 12). For instance, an early report on PL blinking in elongated rod-like nanocrystals and microcrystals of $MAPbI_3$ perovskite shows multi-state PL fluctuations with large amplitudes (Fig. 11), which become pronounced at lower excitation intensities.[38] Super-resolution localization microscopy technique reveals different intensity levels (or steps) in the multi-state blinking of a rod-like nanocrystal and correlates blinking to different emission localization positions in the crystal. On the other hand, single quantum emitter such as chalcogenide QD shows ON and OFF states. Such blinking in halide perovskite is attributed to photoinduced activation and deactivation of emitting or quenching sites formed by geometrical distortions or the presence of different chemical structures. The quenching sites are analogous to charge traps or crystal defects. As shown in Fig. 12a, during ON state, either the whole nanocrystal is emissive with the emission localization position at the centre of the crystal (quenching site model) or PL comes from different positions acting as emitting sites in the crystal (emitting site model). In quenching site model [Fig. 12a (i)], a photogenerated quencher acts as the charge trap, which is formed at the ends of a rod-like perovskite nanocrystal. This quencher deactivates all the photogenerated electrons and holes. As a result, a decrease in PL intensity and a shift of emission localization position, marking a 'step' with intermediate PL intensity or OFF state, is observed. On the other hand, in emitting site model [Fig. 12a (ii)], all the charge carriers in the crystal diffuse efficiently to the emitting sites and recombine radiatively (ON state). If one of the emitting sites is deactivated or quenched, the PL intensity drops and the localization position shifts ('steps' with intermediate PL intensity or OFF state). Alternatively, PL blinking can be assigned to the formation of quenchers near to the emitting sites or by changing the emitting site to a quencher.[38] The enhancement of PL intensity and decrease of amplitude associated

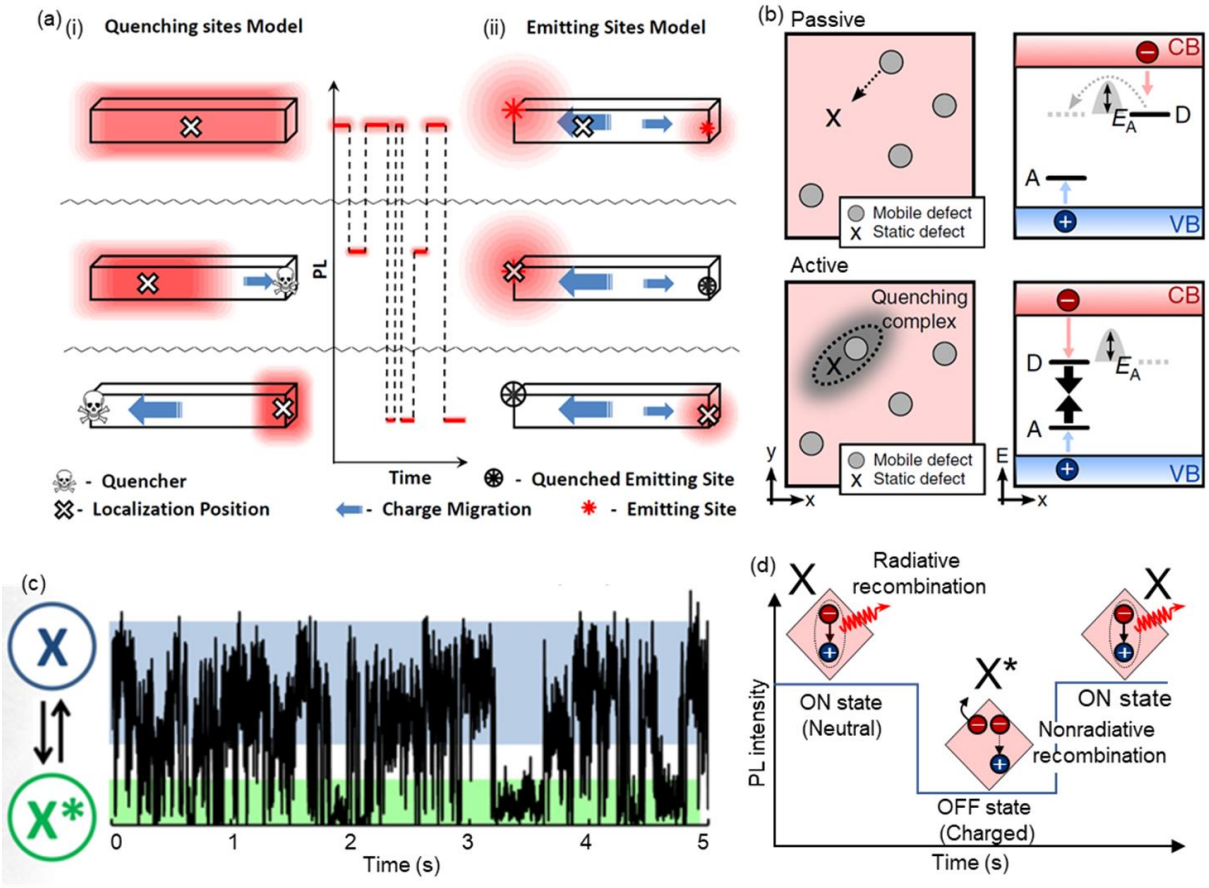

Fig. 12 The origin of PL blinking in perovskites. (a) Quenching and emitting sites models of blinking in nano- and micro- crystals. (b) The formation and active-passive state switching of quenching complex during PL blinking in nanocrystals. (c) A PL intensity trajectory showing two-state blinking in a $CsPbI_3$ perovskite QD. (d) Photoinduced charging-discharging model of two-state blinking in perovskite QD. Reproduced with permission from (a) ref. 38 (copyright 2015, American Chemical Society), (b) ref. 39 (copyright 2019, Nature Publishing Group), and (c) ref. 41 (copyright 2015, American Chemical Society).

with an increase in excitation power density can be attributed to defect- or trap-filling. The high concentration of charge carriers generated at high excitation intensity leads to PL intensity averaging over many emitting sites.

Blinking by photoinduced activation-deactivation of charge traps is supported by temperature-dependent PL measurements of $MAPbI_3$ nanocrystals, correlating blinking with random switching model of quenchers or switching of charge traps between the active and passive states (Fig. 12b).[39] The switching of quenchers is thermally activated, which is supported by suppressed blinking at low temperatures. This blinking suppression is due to the poor diffusion of quenching sites. Although the thermal barrier for the activation of quenching sites is in the order of activation energy for halide migration,[39] quenching by the migration of halide or proton alone cannot model PL blinking. Thus, blinking is discussed in terms of a

"quenching complex" which is a combination of shallow mobile (or localized) electron trap present near to the conduction band and a localized (or mobile) hole trap near to the valence band (Fig. 12b). However, such individual shallow defects are unlikely to cause blinking.

PL blinking is observed in perovskite microcrystals and nanocrystals even at low excitation intensities, where the nonradiative Auger process is negligible. This behaviour contradicts with the origin of PL blinking of chalcogenide QDs at higher excitation intensities/energies, which involves photoinduced charging and neutralization. This difference between the blinking behaviour of perovskite nanocrystals and chalcogenide QDs is due to the weakly-confined charge carriers in large perovskite crystals. In contrast, like chalcogenide QDs, single perovskite QDs show two-state PL blinking (Fig. 12c) due to random charging by photoionization and subsequent neutralization.[41] This type of blinking is called type-A blinking. At higher excitation intensities, blinking becomes more pronounced with prolonged OFF, which is attributed to an increase in rates of photoionization and nonradiative Auger recombination process. As shown in Fig. 12d, charged excitonic state, called a trion (X*), represents OFF state and the neutral (X) state represents ON state. The significant decrease in PL lifetime during OFF state (ca 0.78 ns) of $CsPbI_3$ perovskite QDs when compared to ON state (ca 13.2 ns) confirms type-A blinking.[41] Perovskite QDs also show type-B blinking which is characterized by the repeated activation and deactivation of trap.[42]

Apart from charge- and defect-induced blinking, PL properties of perovskites single particles are affected by oxygen and moisture. Both photobleaching[42] and photobrightening[37,38] are observed under ambient conditions. For example, a decrease in PL intensity of $MAPbI_3$ nanocrystals is observed in air than in argon or polymer environment (Fig. 13a).[40] Such a decrease is attributed to self-sensitized generation of superoxide and the subsequent oxidative disintegration of $MAPbI_3$ nanocrystals (Fig. 13b). Interestingly, PL intensity recovers after long OFF intervals [Fig. 13a (iv)], showing that ultrafast nonradiative Auger recombination processes during the OFF state prevent electron transfer to oxygen, the generation of superoxide, and oxidation of $MAPbI_3$ nanocrystals. On the other hand, oxidation persists throughout the neutral or ON state, showing that the rate of superoxide generation exceeds radiative relaxation. Single particle studies help one to address photooxidation and photostability of perovskites.

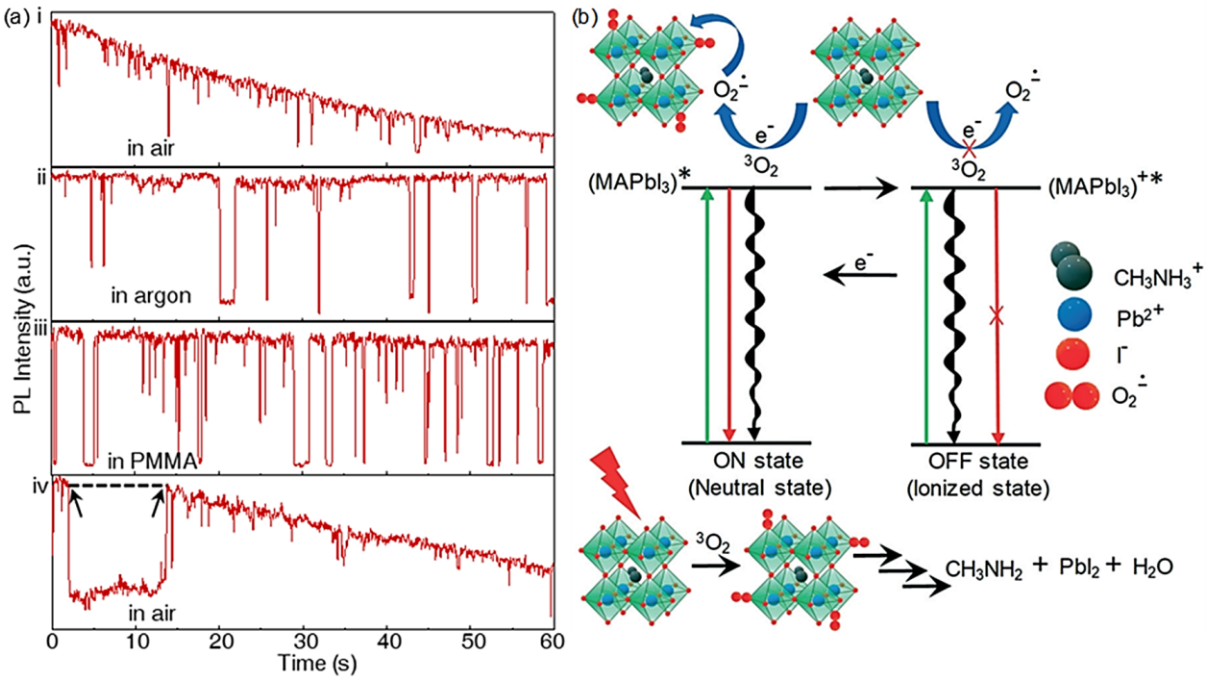

Fig. 13 The effect of local environment on PL blinking of $MAPbI_3$ single nanocrystals. (a) PL intensity trajectories (i) at air/glass interface, (ii) in argon atmosphere, (iii) in a poly(methyl methacrylate) (PMMA) film, and (iv) at air/glass interface showing recovery of PL intensity after a long OFF state. (b) A scheme of (upper part) superoxide generation by a $MAPbI_3$ nanocrystal, (middle part) radiative and nonradiative processes associated with various states, and (lower part) superoxide-mediated disintegration of a $MAPbI_3$ nanocrystal. Reproduced with permission from ref. 40 (copyright 2019, Wiley-VCH Verlag GmbH & Co. KGaA, Weinheim).

6. Applications

6.1. Solar Cell

Perovskites are promising materials for solar cells, which is owing to their high absorption coefficient, long diffusion length of charge carriers, defect tolerance and low exciton binding energy. PSC was first reported by Miyasaka and coworkers,[4] where the power conversion efficiency (PCE) was 3.8%. They replaced organic dyes in dye-sensitized solar cells with $MAPbI_3$ perovskite on mesoporous TiO_2 electrodes. After PCE exceeding 10% was achieved using solid-state $MAPbI_3$ PSC, this research attracted much attention of physicists and chemists to engineer cost-effective solar cells. For an efficient PSC, the quality of perovskite layer and defect-free interfacial structure are very important. Various techniques of device fabrication and optimization of hole and electron transfer processes helped the rapid advancement of PSCs. For example, Spiccia and co-workers[15] achieved PCE as high as 13.9% by using micro-crystalline $MAPbI_3$ perovskite film free from grain-boundaries. Subsequently, PCE was increased to >15% with the use of mixed $MAPbI_3$ and $MAPbI_{3-x}Cl_x$ perovskites,[16] >20% with

the use of $MAPbI_3$ perovskite and blade-coating method,[18] and >23%[14] with the use of mixed cation (MA/FA) and mixed halide (Br/I). More recently, the efficiency of PSC is increased up to 25.2% (NREL efficiency chart) which, along with the cost-effective device fabrication, prompts several researchers to commercialize these devices. A comprehensive review on the background of PSC and the recent progress in PSC fabrication is available elsewhere.[17]

Typical PSC architecture as shown in Fig. 14a, has a perovskite layer as the intrinsic light

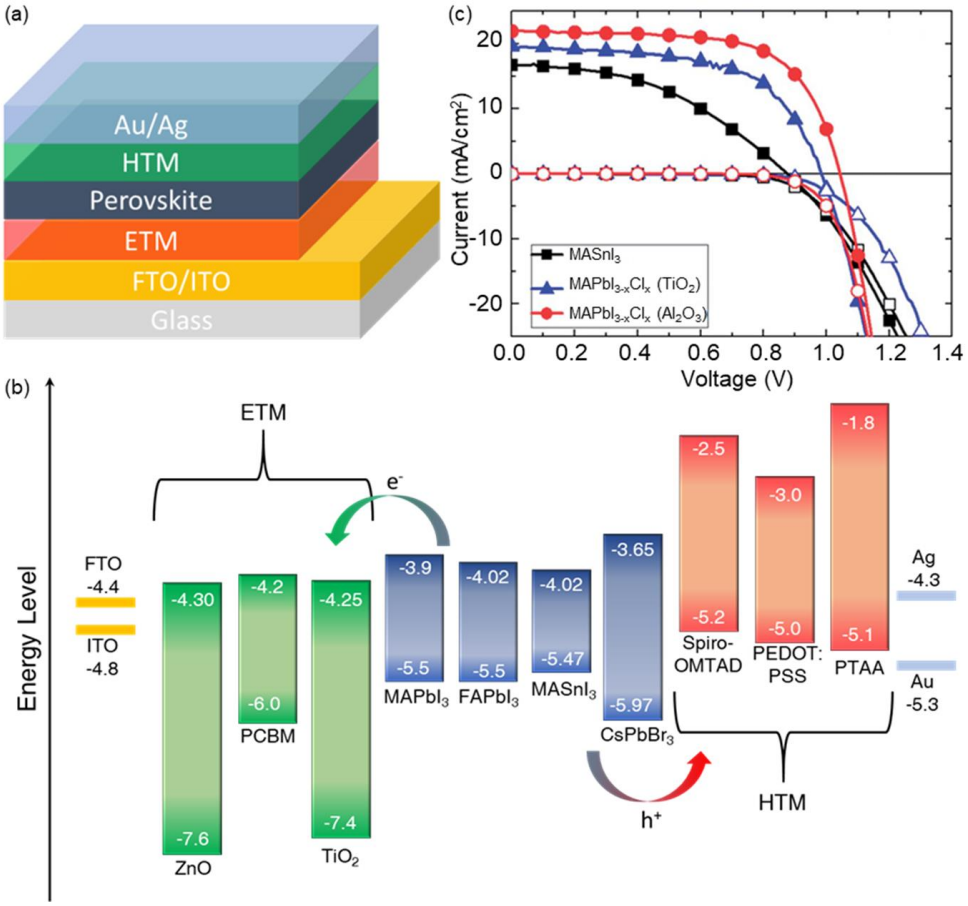

Fig. 14 Characteristics of perovskite solar cells. (a) Device architecture of a PSC. (b) Energy levels of various electron transport, hole transport, perovskite and electrode materials. (c) Current-voltage curves of lead- and tin-based PSCs. Fig. c is reproduced with permission from ref. 13 (copyright 2014, The Royal Society of Chemistry).

absorbing semiconductor sandwiched in between the electron transport materials (ETM) and hole transport materials (HTM) on a fluorine-doped tin oxide (FTO) or ITO glass substrate. TiO_2 or [6,6]-phenyl-C_{61}-butyric acid methyl ester (PCBM) is common *n*-type ETM and 2,2′,7,7′-tetrakis(*N*,*N*-dimethoxyphenylamine)-9,9′-spirobifluorene (spiro-OMTAD) or poly(3,4-ethylenedioxythiophene)−polystyrene sulfonate (PEDOT:PSS) is common *p*-type HTM. Following the absorption of light by the perovskite layer, photogenerated electrons are transferred to the conduction band of ETM and subsequently to FTO/ITO. Hole is transferred

to the valence band of HTM and then to the Au/Ag layer. One can design efficient solar cells by selecting perovskites, HTMs and ETMs by referring to the energy states and bandgaps in Fig. 14b. ETM and HTM in Fig. 14b are selected to facilitate efficient electron and hole transport from photoexcited perovskites.

The low exciton binding energy and the ambipolar charge carrier mobility render PSCs with *p-i-n* or *n-i-p* junction. Thus, charge carriers can be extracted even without any HTM or ETM. However, HTM and ETM are needed for high efficiency PSCs because the open circuit voltage (V_{OC}), current density (J_{SC}) and fill factor in a solar cell are determined by these materials. As a result, recently spiro-OMTAD has been replaced by a fluorine-terminated HTM, where the durability and PCE of a $(FAPbI_3)_{0.95}(MAPbBr_3)_{0.05}$ PSC are 500 h and >23%, respectively.[14] Highly stable PSCs with high PCEs can be fabricated using perovskites with triple/quadruple cations. Also, lead-free PSCs are promising in terms of their performance and efficiency. Although Sn^{2+} is the most promising substitute of Pb^{2+}, the instability of Sn^{2+} against oxidation is the challenging issue. Snaith and co-workers reported >6% PCE and >0.88 V_{OC} in a $MASnI_3$-based solar cell (Fig. 14c).[13] Recently, Hayase and co-workers stabilized Sn-based PSC by doping with Ge, and sustained PCE at 6.9%.[43] To ensure the stability of PSCs against heat, humidity, and light, studies focus on improvement of interfacial structures at grain boundaries and junction.[14,17,18,43] The device stability is also highly affected by the quality of HTMs which generally contain diffusible dopants. An important direction of PSC is to use all inorganic compositions of perovskites as absorbers having high thermal stability.

In photovoltaic community, perovskites have evolved as promising materials for high efficiency solar cells despite the challenges in their stability. The highly ionic nature of perovskite lattice results in degradation of the lattice and leakage of Pb^{2+} cation in the presence of moisture. Further, photo-ionic conductivity of halides and metal ions limits the performance of PSCs. Nevertheless, there is enough room to address all these challenges and improve the performance of PSCs to their optimal level.

6.2. LED

Tuneable PL and high PLQY of perovskites attract people to fabricate multicolor perovskite LEDs (PeLEDs).[1,44-46] The low defect density and ambipolar carrier migration in these materials enable efficient injection and transport of charges across the interfaces, ameliorating the device performance. Although the attempts to use halide perovskites in LEDs date back to early 90's, room temperature multicolor PeLED was realized only very recently. Recently, the (peak) external quantum efficiencies (EQEs) of green (20.3%)[45] and red (21.6%)[1]

PeLED are considerably improved. Pure chloride and mixed chloride-bromide perovskites are employed in blue PeLEDs. For example, by using $CsPb(Br/Cl)_3$ NCs, Kovalenko and coworkers developed a blue PeLED with 1.2% EQE at 4.4 mA/cm^2.[44] The structure and electroluminescence (EL) spectra of the blue LED are shown in Fig. 15 a and b, respectively. Although the EL wavelength of this LED remains constant at 463 nm (Fig. 15c), the EL intensity monotonously decreased with time. Thus, blue PeLEDs research is open to improve EQE and the stability.

Typical device structure of a PeLED consists of a light-emitting layer of halide perovskites placed in between the charge (electron and hole) injection (transfer) layers and electrodes. Halide perovskites in their polycrystalline thin film or nanostructure (nanocrystals, platelets or QDs) forms form double heterojunctions with the charge injection layers. As shown in Fig. 14b and discussed in 'Solar cells' section, the charge injection layers are large bandgap semiconductors which enable efficient and balanced injection and confinement of charge carriers. PeLED devices are fabricated with the configuration of ITO/PEDOT:PSS/halide perovskite/B3PYMPM/LiF/Al as shown in Fig. 15.[44] Here, PEDOT:PSS acts as the hole-transport layer, B3PYMPM is the electron-transport layer, LiF is the electron-injection layer, and ITO and Al are anode and cathode, respectively. Record-breaking EQE (20.3%)[45] can be achieved with such a configuration by incorporating a thin layer of insulating PMMA in between the perovskite layer and electron-transport layer.

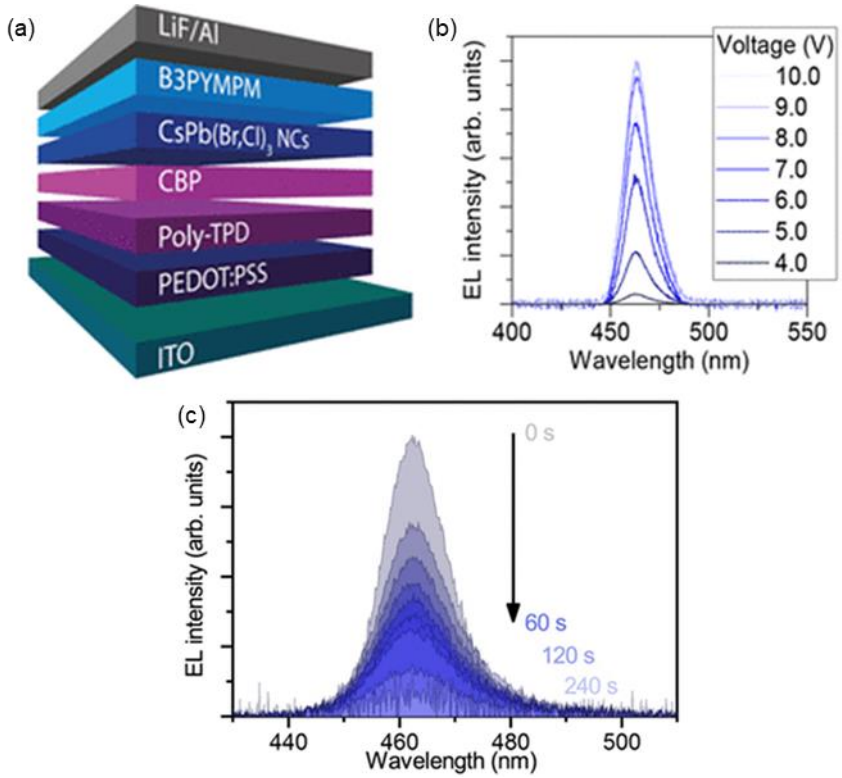

Fig. 15 EL characteristics of a blue PeLED. (a) Device structure of the PeLED, (b) EL spectra of the PeLED at various applied voltages, and (c) EL spectra recorded at 5 V and different time. Reproduced with permission from ref. 44 (copyright 2019, American Chemical Society).

The intrinsic stability of halide perovskites and the efficiency of PeLEDs are influenced by the crystal structure, temperature, atmosphere, and light. Other factors detrimental to the performance of PeLED are unbalanced charge injection and transport across the perovskite/electron-transport layer or perovskite/hole-transport layer interfaces, the current leakage due to pinholes in the perovskite layer, and nonradiative losses in the perovskite layer. While the balanced charge injection and transport are achieved by the proper selection of electron- and hole-transport layers and modification of perovskite/charge-injection interfaces, the current leakage can be lifted-up by increasing the surface coverage and decreasing the surface roughness of perovskite layer. The suppression of nonradiative recombination under an electrical bias is another important factor to achieve high-performance PeLEDs. For example, a PeLED device with record-breaking 20.3% EQE and 80% PLQY is fabricated using compositionally graded quasi-core/shell $CsPbBr_3$/MABr perovskite layer.[45] Here, MABr passivates the nonradiative defect sites, increases the PL lifetime and the surface coverage, and balances charge injection. In organic-inorganic hybrid perovskites, an interesting strategy of defect passivation is the use of molecules with high affinity to defect sites. For example, EQE

as high as 21.6% is achieved for a $FAPbI_3$-based NIR PeLED, which is by passivating defects using 2,2′-[oxybis(ethylenoxy)]diethylamine.[1]

Besides the passivation of defects, one of the successful approaches to enhance EQE is to use low-dimensional perovskite structures such as nanocrystals, platelets, quasi-2D/3D nanostructures, and QDs. EQE of PeLEDs constructed using bulk perovskite layers or films is limited by the thermal dissociation of excitons, which suppresses monomolecular or geminate-type excitonic recombination. Further, the bimolecular recombination kinetics in halide perovskites follow a quadratic relation with the charge carrier density, *i.e.* n^2. Therefore, the radiative recombination in such perovskite layers becomes important only at higher charge densities. Nanostructure perovskites lift these problems by enhancing the monomolecular radiative recombination through carrier confinement. For example, a red-emitting PeLED with high EQE (21.3%) is constructed by using anion-exchanged perovskite QDs.[46] Despite these approaches to improve the performance of PeLEDs, the devices are still behind commercial LEDs due to the poor stability of perovskites in diverse environments.

6.3. Laser

The high PLQY, large absorption cross-section and low defect density of perovskites make these materials promising for lasing. After the successful demonstration of low threshold amplified spontaneous emission (ASE) in solution-processed $CsPbX_3$ (X = Cl, Br, and I) nanocrystals,[2] investigations of lasing and ASE have been extended to various geometrical shapes of MA-, FA- and Cs-based perovskites.[2,20,47-50] With the increase in intensity of excitation light, the emission spectrum changes from broad, spontaneous emission (SE) to a narrow, red-shifted peak with higher intensity, which is the signature of ASE (Fig. 16a).[48] Furthermore, single and multimode lasing with ultranarrow emission band and high quality (Q) factor are realized in perovskites (Fig. 16b).[20,49] The lasing wavelength in these materials can be tuned in the entire visible to NIR region by controlling the halide composition (Fig. 16c).[49] Lasing in all-inorganic, organic-inorganic, and mixed halide perovskites is demonstrated by the arrangement of these materials to form different cavities (Fig. 17), such as random cavity,[2,47] vertical microcavity,[50] Whispering Gallery Mode cavity (WGM),[2,49] and Fabry-Perot cavity.[20]

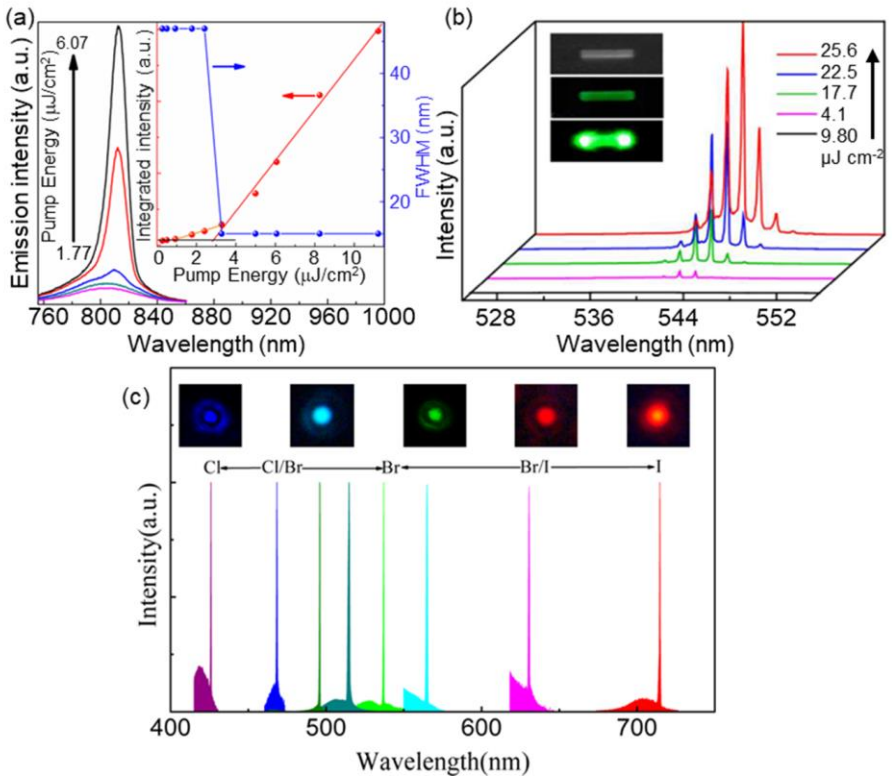

Fig. 16 ASE and lasing in perovskites. (a) ASE in a $FAPbI_3$ film excited with 150 fs laser. Inset: Integrated emission intensity and full width at half maximum (FWHM) as the function of pump energy, showing ASE threshold at 3 μJ cm^{-2}. (b) Triangular rod emission spectra around the lasing threshold. (c) Multicolor, single-mode lasing and the corresponding emission images of $CsPbX_3$ microspheres. Reproduced with permission from (a) ref. 48 (copyright 2017, American Chemical Society), (b) ref. 20 (copyright 2016, American Chemical Society), and (c) ref. 49 (copyright 2017, American Chemical Society).

Perovskite thin films exhibit random lasing. ASE threshold can be lowered, and the optical gain can be improved by improving the quality of the film. For example, ASE threshold is lowered from 3 μJ cm^{-2} to 1.6 μJ cm^{-2} by improving the quality of a $FAPbI_3$ film by treating it with appropriate stoichiometric amounts of MABr and FAI.[48] The propagating SE in the film is amplified by stimulated emission when the intensity of excitation light exceeds certain threshold, resulting in population inversion. During the propagation of emission in the film, the micro/nanodomains present in it produce coherent backscattering and generate closed-loop cavities (Fig. 17a). When the optical gain exceeds the loss, random lasing occurs at the resonant frequency of the corresponding feedback loop. In a $MAPbI_3$ film, random lasing is observed at the threshold of 102 μJ cm^{-2} with high optical gain and strong multiple backscattering provided by the randomly arranged polycrystalline grain boundaries.[47]

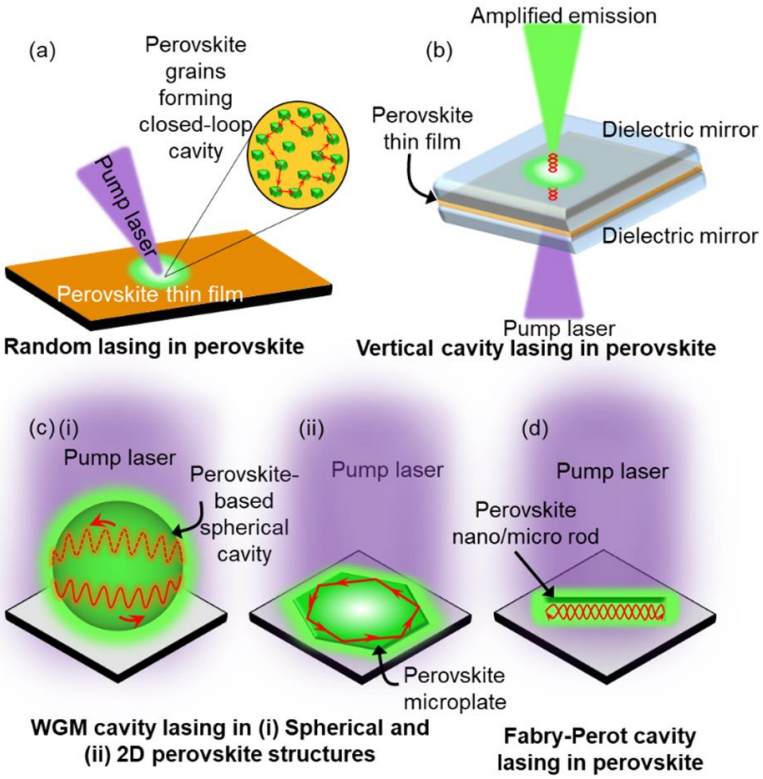

Fig. 17 Lasing cavities in perovskites. (a) Random cavity, (b) vertical cavity, (c) WGM cavity, and (d) Fabry-Perot cavity.

Cavity lasing is achieved by constructing vertical (Fig. 17b), WGM (Fig. 17c) or Fabry-Perot (Fig. 17d) cavities. Vertical cavity is prepared by sandwiching a perovskite film in between two gallium nitride distributed Bragg's reflector mirrors. The resonators suppress most of the optical states and allow emission from a few states, resulting in mode-controlled lasing. Recently, ultralow lasing threshold of 0.39 μJ cm^{-2} is reported for $CsPbBr_3$ QD vertical cavity.[50] Similarly, WGM lasing is attained either in perovskite microspheres[49] or by coating perovskite nanocrystals on substrates such as silica microspheres.[2] Here, the substrates form circular cavities in which the total internal reflection occurs around the circumference [Fig. 17c(i)]. Ultralow threshold (~0.42 μJ cm^{-2}) single-mode WGM lasing occurs in a $CsPbX_3$ microsphere cavity with narrow line width (~0.09 nm) and high Q factor (~6100).[49] WGM lasing is observed in various 2D structures as well when the emission is confined within their boundaries [Fig. 17c(ii)]. Fabry-Perot lasing is observed in perovskite nanocuboids, micro-nano rods, and wires. Such structures act as optical waveguides along the axial or planar direction and create a Fabry–Perot cavity by confining the light *via* total internal reflection at the two end facets. Multi-mode Fabry−Perot lasing at room temperature, with low lasing thresholds (~14.1 μJ cm^{-2}) and high Q-factor (~3500) is achieved in $CsPbX_3$ rods.[20] The lasing

threshold in Fabry-Perot cavities vary largely, depending on the shape, size, end facets, crystalline quality and halide composition.

Despite the tunable lasing color and low lasing threshold of perovskite lasers, the exact mechanism of optical gain is yet to be rationalized. In organic-inorganic perovskites, the majority of photogenerated charge carriers are free, and the population of bound excitons is negligibly small due to the small exciton binding energy. The concentration of free charge carriers that fill certain states increases as the intensity of excitation light increases, providing a necessary condition for optical gain by population inversion. On the other hand, in all-inorganic perovskites, the optical gain and ASE are assigned to the radiative recombination of biexcitons.

7. Summary and Outlook

With the straightforward synthesis, halide perovskites emerge into one of the most promising classes of semiconductor materials for solar cells, lasers, LEDs, and photodetectors. The fascinating optical and electronic properties of perovskites originate from weekly-bound excitons activated in the band-edge states which are formed by the hybridization of halide orbitals with B-site metal ion orbitals. Thus, optical and electronic properties of perovskites strongly depend on halide composition, and their optical absorption and emission color are tuned throughout the visible to near-infrared region by synthesizing pure or mixed halide perovskites. Further, these properties can be modified by varying the temperature and pressure, changing the composition of A-site and B-site cations, and controlling the size and shape of crystals. For example, emission wavelength and spectral width, charge carrier lifetime, and exciton binding energy can be modified by downsizing perovskites from macroscopic films and microscale crystals to nanocrystals and quantum dots. The excellent abilities of perovskites to absorb light, which is followed by the generation and long-range diffusion of free charge carriers, make them attractive to solar cells. Further, perovskites, owing to the tunable excitonic emission wavelength and high photoluminescence quantum yields, find applications to high efficiency, multicolor LEDs and low threshold, multicolor lasers. Although lead perovskites show excellent optoelectronic properties and device performances, the environmental and health costs of lead encourage researchers to develop lead-free perovskites by selecting B-site cations from among Cu^{+}, Ag^{+}, Sn^{2+}, Ge^{2+}, Bi^{3+}, In^{3+} and Sb^{3+}. Another important challenge in this field is the poor stability of perovskites against moisture and oxygen. Thus, much effort has been dedicated to stabilizing perovskites with shells from materials such as polymers and silica. Commercial devices and biological applications of halide perovskites can be realized

with the development of non-toxic perovskites with optimized structure, stability, and optical and charge carrier properties, which cannot be too far.

Notes

The authors declare no competing financial interest.

Acknowledgments

VB Acknowledges support under the MEXT JSPS Grant-in-Aid for Scientific Research B (19H02550), MEXT JSPS Special Advancement Research Grant (18H05205), and MEXT JSPS Dynamic Alliance for Open Innovation Bridging Human, Environment and Materials. VB and CS acknowledge support under the Scheme for Promotion of Academic and Research Collaboration (SPARC) by Science Engineering of Board of India. CS acknowledges Japan International Cooperation Agency (JICA) for financial support. LC acknowledges JICA Scholarship for doctoral research and SG acknowledges MEXT Scholarship for doctoral research.

References

1. W. Xu, Q. Hu, S. Bai, C. Bao, Y. Miao, Z. Yuan, T. Borzda, A. J. Barker, E. Tyukalova, Z. Hu et al., *Nat. Photonics.*, 2019, **13**, 418−424.
2. S. Yakunin, L. Protesescu, F. Krieg, M. I. Bodnarchuk, G. Nedelcu, M. Humer, G. D. Luca, M. Fiebig, W. Heiss and M. V. Kovalenko, *Nat. Commun.*, 2015, **6**, 8056.
3. B. Pradhan, G. S. Kumar, S. Sain, A. Dalui, U. K. Ghorai, S. K. Pradhan and S. Acharya, *Chem. Mater.*, 2018, **30**, 2135-2142.
4. A. Kojima, K. Teshima, Y. Shirai and T. Miyasaka, *J. Am. Chem. Soc.*, 2009, **131**, 6050−6051.
5. S. D. Stranks, G. E. Eperon, G. Grancini, C. Menelaou, M. J. P. Alcocer, T. Leijtens, L. M. Herz, A. Petrozza and H. J. Snaith, *Science*, 2013, **342**, 341−344.
6. I. Levchuk, A. Osvet, X. Tang, M. Brandl, J. Perea, F. Hoegl, G. J. Matt, R. Hock, M. Batentschuk and C. J. Brabec, *Nano Lett.*, 2017, **17**, 2765−2770.
7. M. I. Saidaminov, A. L. Abdelhady, G. Maculana and O. M. Bakr, *Chem. Commun*., 2015, **51**, 17658−17661.
8. S. Ghimire, L. Chouhan, Y. Takano, K. Takahashi, T. Nakamura, K. Yuyama and V. Biju, *ACS Energy Lett.*, 2019, **4**, 133−141.

9. T. C. Jellicoe, J. M. Richter, H. F. J. Glass, M. Tabachnyk, R. Brady, S. E. Dutton, A. Rao, R. H. Friend, D. Credgington, N. C. Greenham and M. L. Böhm, *J. Am. Chem. Soc.*, 2016, **138**, 2941−2944.
10. J. S. Manser, J. A. Christians and P. V. Kamat, *Chem. Rev.*, 2016, **116**, 12956−13008.
11. J. Zhang, Y. Yang, H. Deng, U. Farooq, X. Yang, J. Khan, J. Tang and H. Song, *ACS Nano*, 2017, **11**, 9294−9302.
12. E. T. McClure, M. R. Ball, W. Windl and P. M. Woodward, *Chem. Mater*., 2016, **28**, 1348−1354.
13. N. K. Noel, S. D. Stranks, A. Abate, C. Wehrenfennig, S. Guarnera, A.-A. Haghighirad, A. Sadhanala, G. E. Eperon, S. K. Pathak, M. B. Johnston et al., *Energy Environ. Sci.*, 2014, **7**, 3061−3068.
14. N. J. Jeon, H. Na, E. H. Jung, T. Yang, Y. G. Lee, G. Kim, H. Shin, S. I. Seok, J. Lee and J. Seo, *Nature Energy*, 2018, **3**, 682−689.
15. M. Xiao, F. Huang, W. Huang, Y. Dkhissi, Y. Zhu, J. Etheridge, A. Gray-Weale, U. Bach, Y. Cheng and L. Spiccia, *Angew. Chem.*, 2014, **126**, 10056−10061.
16. J.-H. Im, I. Jang, N. Pellet, M. Grätzel and N. Park, *Nature Nanotechnol.*, 2014, **9**, 927−932.
17. A. K. Jena, A. Kulkarni and T. Miyasaka, *Chem. Rev.*, 2019, **119**, 3036−3103.
18. Y. Deng, X. Zheng, Y. Bai, Q. Wang, J. Zhao and J. Huang, *Nature Energy*, 2018, **3**, 560−566.
19. D. Shi, V. Adinolfi, R. Comin, M. Yuan, E. Alarousu, A. Buin, Y. Chen, S. Hoogland, A. Rothenberger, K. Katsiev et al., *Science*, 2015, **347**, 519−522.
20. H. Zhou, S. Yuan, X. Wang, T. Xu, X. Wang, H. Li, W. Zheng, P. Fan, Y. Li, L. Sun and A. Pan, *ACS Nano*, 2017, **11**, 1189−1195.
21. L. Protesescu, S. Yakunin, M. I. Bodnarchuk, F. Bertolotti, N. Masciocchi, A. Guagliardi, and M. V. Kovalenko, *J. Am. Chem. Soc.*, 2016, **138**, 14202−14205.
22. F. Zhang, H. Zhong, C. Chen, X. Wu, X. Hu, H. Huang, J. Han, B. Zou and Y. Dong, *ACS Nano*, 2015, **9**, 4533−4542.
23. B. Yang, X. Mao, F. Hong, W. Meng, Y. Tang, X. Xia, S. Yang, W. Deng and Keli Han, *J. Am. Chem. Soc.*, 2018, **140**, 17001−17006.
24. L. Protesescu, S. Yakunin, M. I. Bodnarchuk, F. Krieg, R. Caputo, C. H. Hendon, R. X. Yang, A. Walsh and M. V. Kovalenko, *Nano Lett.*, 2015, **15**, 3692−3696.
25. L. Wang, N. E. Williams, E. W. Malachosky, J. P. Otto, D. Hayes, R. E. Wood, P. Guyot-Sionnest and G. S. Engel, *ACS Nano*, 2017, **11**, 2689−2696.

26. M. I. Saidaminov, A. L. Abdelhady, B. Murali, E. Alarousu, V. M. Burlakov, W. Peng, I. Dursun, L. Wang, Y. He, G. Maculan, A. Goriely et al., *Nat. Commun.*, 2015, **6**, 7586.
27. L. Huang and W. R. L. Lambrecht, *Phys. Rev., B*, 2013, **88**, 165203.
28. Q. A. Akkerman, S. G. Motti, A. R. S. Kandada, E. Mosconi, V. D'Innocenzo, G. Bertoni, S. Marras, B. A. Kamino, L. Miranda, F. D. Angelis et al., *J. Am. Chem. Soc.*, 2016, **138**, 1010−1016.
29. Q. Dong, Y. Fang, Y. Shao, P. Mulligan, J. Qiu, L. Cao and J. Huang, *Science*, 2015, **347**, 967−970.
30. R. L. Milot, G. E. Eperon, H. J. Snaith, M. B. Johnston and L. M. Herz, *Adv. Funct. Mater.*, 2015, **25**, 6218−6227.
31. C. Wehrenfennig, G. E. Eperon, M. B. Johnston, H. J. Snaith and L. M. Herz, *Adv. Mater.*, 2014, **26**, 1584−1589.
32. A. Amat, E. Mosconi, E. Ronca, C. Quarti, P. Umari, Md. K. Nazeeruddin, M. Grätzel and F. D. Angelis, *Nano Lett.*, 2014, **14**, 3608−3616.
33. Y. Dong, T. Qiao, D. Kim, D. Parobek, D. Rossi and D. H. Son, *Nano Lett.*, 2018, **18**, 3716−3722.
34. V. Malgras, S. Tominaka, J. W. Ryan, J. Henzie, T. Takei, K. Ohara and Y. Yamauchi, *J. Am. Chem. Soc.*, 2016, **138**, 13874−13881.
35. D. Zhang, Y. Yu, Y. Bekenstein, A. B. Wong, A. P. Alivisatos and P. Yang, *J. Am. Chem. Soc.*, 2016, **138**, 13155−13158.
36. L. Wang, K. Wang and B. Zou, *J. Phys. Chem. Lett.*, 2016, **7**, 2556−2562.
37. C. Li, Y. Zhong, C. A. M. Luna, T. Unger, K. Deichsel, A. Gräser, J. Köhler, A. Köhler, R. Hildner and S. Huettner, *Molecules*, 2016, **21**, 1081.
38. Y. Tian, A. Merdasa, M. Peter, M. Abdellah, K. Zheng, C. S. Ponseca, Jr., T. Pullerits, A. Yartsev, V. Sundström and I. G. Scheblykin, *Nano Lett.*, 2015, **15**, 1603−1608.
39. M. Gerhard, B. Louis, R. Camacho, A. Merdasa, J. Li, A. Kiligaridis, A. Dobrovolsky, J. Hofkens and I. G. Scheblykin, *Nat. Commun.*, 2019, **10**, 1698.
40. L. Chouhan, S. Ghimire and V. Biju, *Angew. Chem. Int. Ed.*, 2019, **58**, 4875−4879.
41. Y.-S. Park, S. Guo, N. S. Makarov and V. I. Klimov, *ACS Nano*, 2015, **9**, 10386−10393.
42. G. Yuan, C. Ritchie, M. Ritter, S. Murphy, D. E. Gómez and Paul Mulvaney, *J. Phys. Chem. C*, 2018, **122**, 13407−13415.
43. N. Ito, M. A. Kamarudin, D. Hirotani, Y. Zhang, Q. Shen, Y. Ogomi, S. Iikubo, T. Minemoto, K. Yoshino and S. Hayase, *J. Phys. Chem. Lett.*, 2018, **9**, 1682−1688.

44. S. T. Ochsenbein, F. Krieg, Y. Shynkarenko, G. Rainò and M. V. Kovalenko, *ACS Appl. Mater. Interfaces*, 2019, **11**, 21655−21660.
45. K. Lin, J. Xing, L. N. Quan, F. P. G. de Arquer, X. Gong, J. Lu, L. Xie, W. Zhao, D. Zhang, C. Yan, et al., *Nature*, 2018, **562**, 245−248.
46. T. Chiba, Y. Hayashi, H. Ebe, K. Hoshi, J. Sato, S. Sato, Y.-J. Pu, S. Ohisa and J. Kido, *Nat. Photonics*, 2018, **12**, 681−667.
47. Z.-F. Shi, X.-G. Sun, D. Wu, T.-T. Xu, Y.-T. Tian, Y.-T. Zhang, X.-J. Li and G.-T. Du, *J. Mater. Chem. C*, 2016, **4**, 8373−8379.
48. F. Yuan, Z. Wu, H. Dong, J. Xi, K. Xi, G. Divitini, B. Jiao, X. Hou, S. Wang and Q. Gong, *J. Phys. Chem. C*, 2017, **121**, 15318−15325.
49. B. Tang, H. Dong, L. Sun, W. Zheng, Q. Wang, F. Sun, X. Jiang, A. Pan and L. Zhang, *ACS Nano*, 2017, **11**, 10681−10688.
50. C.-Y. Huang, C. Zou, C. Mao, K. L. Corp, Y.-C. Yao, Y.-J. Lee, C. W. Schlenker, A. K. Y. Jen and L. Y. Lin, *ACS Photonics*, 2017, **4**, 2281−2289.

Lata Chouhan studied chemistry at Indian Institute of Technology, Bombay. She was awarded a JICA fellowship in 2017 for doctoral research in Hokkaido University. First, she was a JICA research student during October 2017 to March 2018. Since April 2018, she is a PhD student under the guidance of Vasudevanpillai Biju in Hokkaido University. She focuses her research on single particle microscopy and spectroscopy for the control of charge carrier and exciton recombination in nanocrystals and quantum dots of lead halide perovskite.

Sushant Ghimire studied chemistry at Tribhuvan University in Nepal. In 2016, he was awarded a MEXT Scholarship for doctoral research in Hokkaido University. He was a MEXT research student during April 2016 to March 2017 and a PhD student during April 2017 to March 2020 under the guidance of Vasudevanpillai Biju in Hokkaido University. His research focuses on the dynamics of charge carriers in perovskite nanocrystals, assembles, and thin films.

Challapally Subrahmanyam obtained his PhD degree in Chemistry from Indian Institute of Technology Madras in 2003. During 2003 to 2007, he was a postdoctoral fellow in École polytechnique fédérale de Lausanne, Switzerland. He started his academic career as an assistant professor in National Institute of Technology Trichy, India. In 2009, he moved in Indian Institute of Technology Hyderabad as an assistant professor, where he is currently a professor of chemistry and the dean academic affairs. His research focuses on nanomaterials for solar energy harvesting and environmental remediation.

Tsutomu Miyasaka obtained his undergraduate degree in Applied Chemistry from Waseda University in March 1976 and Master's degree in industrial chemistry from the University of Tokyo in 1978. He continued his studied at the university of Tokyo and obtained his PhD in 1981. Also, during this time, he was a visiting researcher at the University of Quebec in Canada. After obtaining his PhD, he joined Fujifilm where he worked on the development of high-sensitivity films for photo camera films for instant cameras and the development of lithium-ion battery. In 2001, he became a professor at Graduate School of Engineering at Toin University of Yokohama where he established Peccell Technologies for solar cells and was the representative director until 2009. Also, he is a visiting professor at Research Centre for Advanced Science and Technology, The University of Tokyo. Since the first demonstration of perovskite solar cell by him in 2009, he has been focussing his research on this subject. He is the recipient of Clarivate Citation Award in 2017.

Vasudevanpillai Biju studied chemistry at National Institute of Interdisciplinary Science and Technology and the University of Kerala and obtained his PhD in 2000. After postdoctoral research in Japan and USA, he was a scientist and senior scientist at Health Research Institute in AIST, Japan. In parallel, he was a PRESTO Researcher of Japan Science and Technology Agency (JST). Since February 2016, he is a professor at Hokkaido University. His current research interests include semiconductor nanocrystals, photo-functional molecules, and single-molecule spectroscopy and microscopy. His research activities are recognized with various awards by Ozaki Foundation (Gen-nai Award), Japanese Photochemistry Association, Asian and Oceanian Photochemistry Association and the Chemical Society of Japan. Since 2011 he is a Fellow of Royal Society of Chemistry.